A&A 608, A133 (2017)
DOI: 10.1051/0004-6361/201731466

Astronomy & Astrophysics

Gas and dust in the star-forming region ρ Oph A

II. The gas in the PDR and in the dense cores[⋆,⋆⋆]

B. Larsson[1] and R. Liseau[2]

[1] Department of Astronomy, Stockholm University, 106 91 Stockholm, Sweden
e-mail: `bem@astro.su.se`
[2] Department of Space, Earth and Environment, Chalmers University of Technology, Onsala Space Observatory, 439 92 Onsala, Sweden
e-mail: `rene.liseau@chalmers.se`

Received 29 June 2017 / Accepted 25 August 2017

ABSTRACT

Context. The evolution of interstellar clouds of gas and dust establishes the prerequisites for star formation. The pathway to the formation of stars can be studied in regions that have formed stars, but which at the same time also display the earliest phases of stellar evolution, i.e. pre-collapse/collapsing cores (Class -1), protostars (Class 0), and young stellar objects (Class I, II, III).
Aims. We investigate to what degree local physical and chemical conditions are related to the evolutionary status of various objects in star-forming media.
Methods. ρ Oph A displays the entire sequence of low-mass star formation in a small volume of space. Using spectrophotometric line maps of H_2, H_2O, NH_3, N_2H^+, O_2, O I, CO, and CS, we examine the distribution of the atomic and molecular gas in this dense molecular core. The physical parameters of these species are derived, as are their relative abundances in ρ Oph A. Using radiative transfer models, we examine the infall status of the cold dense cores from their resolved line profiles of the ground state lines of H_2O and NH_3, where for the latter no contamination from the VLA 1623 outflow is observed and line overlap of the hyperfine components is explicitly taken into account.
Results. The stratified structure of this photon dominated region (PDR), seen edge-on, is clearly displayed. Polycyclic aromatic hydrocarbons (PAHs) and O I are seen throughout the region around the exciting star S 1. At the interface to the molecular core 0.05 pc away, atomic hydrogen is rapidly converted into H_2, whereas O I protrudes further into the molecular core. This provides oxygen atoms for the gas-phase formation of O_2 in the core SM 1, where $X(O_2) \sim 5 \times 10^{-8}$. There, the ratio of the O_2 to H_2O abundance [$X(H_2O) \sim 5 \times 10^{-9}$] is significantly higher than unity. Away from the core, O_2 experiences a dramatic decrease due to increasing H_2O formation. Outside the molecular core ρ Oph A, on the far side as seen from S 1, the intense radiation from the 0.5 pc distant early B-type star HD 147889 destroys the molecules.
Conclusions. Towards the dark core SM 1, the observed abundance ratio $X(O_2)/X(H_2O) > 1$, which suggests that this object is extremely young, which would explain why O_2 is such an elusive molecule outside the solar system.

Key words. ISM: individual objects: ρ Oph A – ISM: molecules – ISM: abundances – photon-dominated region (PDR) – stars: formation – ISM: general

1. Introduction

The physics and chemistry of star-forming clouds are governed by the competition between the energy input into the cloud and the energy lost through the radiation from the gas and the dust. This ability to cool efficiently is paramount during the gravitational formation of stars and planets and, on a grander scale, of galaxies. The abundance of the major coolants is determined by feedback processes between the atoms, molecules, and dust grains that are present in the media. However, many of these processes are only partially understood and are the focus of intense contemporary research. In this paper, we attempt to disentangle the various interrelations among key atomic and molecular species by analysing their distribution within a star-forming cloud.

We chose as a prime example the nearest region of star formation, i.e. the molecular cloud L 1688 at a distance of 120 pc (Loinard et al. 2008). Major properties of the dark clouds in the constellation of Ophiuchus have been reviewed by Wilking et al. (2008) and, more recently, by White et al. (2015). A dense stellar cluster has been forming over the past one to two million years (Bontemps et al. 2001; Evans et al. 2009; Ducourant et al. 2017), transforming cloud matter into a young stellar population at an overall efficiency of a few percent, but with local excursions to a few tens of percent (Wilking & Lada 1983; Liseau et al. 1995, 1999; Bontemps et al. 2001; Evans et al. 2009). Several intensity maxima in DCO^+ line emission were named "cores" and assigned the capital letters A through F by Loren et al. (1990). Since then, this scheme has been extended (e.g. White et al. 2015; Punanova et al. 2016).

The dense core ρ Oph A attracts our particular attention as it harbours several manifestations of star formation within

---

[⋆] Based on observations with *Herschel* which is an ESA space observatory with science instruments provided by European-led Principal Investigator consortia and with important participation from NASA.

[⋆⋆] The data cubes of Figs. 3–10, 12, and A.1 are only available at the CDS via anonymous ftp to
`cdsarc.u-strasbg.fr` (`130.79.128.5`) or via
`http://cdsarc.u-strasbg.fr/viz-bin/qcat?J/A+A/608/A133`

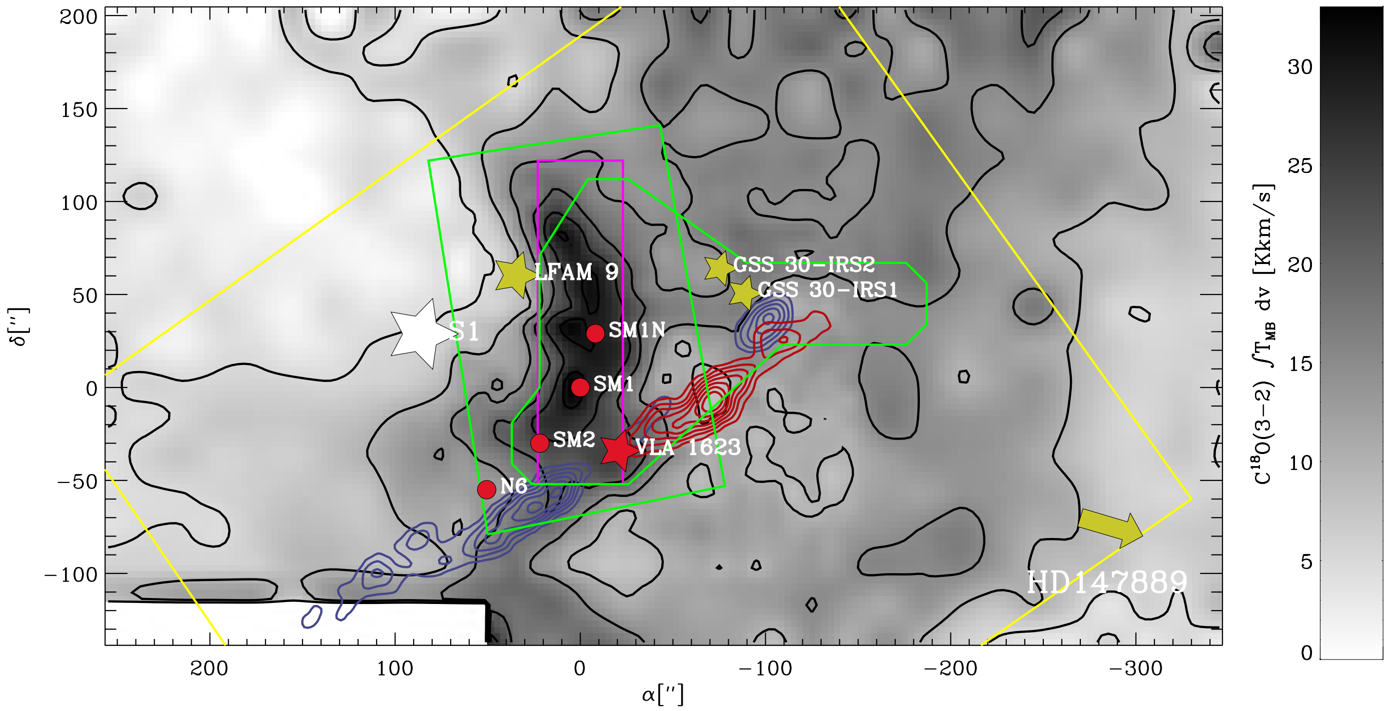

Fig. 1. Regions of our *Herschel* observations in ρ Oph A are superposed onto a greyscale and contour map of $C^{18}O$ (3–2) integrated intensity; see scale bar to the right (Liseau et al. 2010). The region mapped with HIFI in H_2O 557 GHz is shown by the large and partially cut rectangle (yellow; see also Fig. A.1) and that in H_2O 1670 GHz by the small rectangle (magenta). The green rectangle outlines the region mapped with PACS in the [O I] 63, 145 μm lines and in the far-IR continuum. The green polygon marks the perimeter of the O_2 487 GHz observations. Yellow stars identify Class I and II sources, the red star the Class 0 source VLA 1623, and the white star the early-type object S 1 (B4 + K, Gagné et al. 2004). An arrow points towards the 11′ distant early B star HD 147889. The red and blue contours refer to high-velocity gas seen in CO (3–2) emission (JCMT archive). Zero offset is at the position of SM 1, i.e. for J 2000 coordinates RA = $16^{\mathrm{h}}26^{\mathrm{m}}27\overset{\mathrm{s}}{.}9$, Dec = −24°23′57″.

a relatively small volume (length scale approximately 0.1 pc), namely a number of pre-stellar cores, a Class 0 source with its highly collimated molecular jet, and Class I/II sources with their outflows and HH-objects (Fig. 1 and Liseau et al. 2015). In addition, ρ Oph A is prominent for its unique chemistry, including that of O_2, H_2O_2, and HO_2. These were first detected outside the solar system by our group (Larsson et al. 2007; Liseau et al. 2012; Bergman et al. 2011a; Parise et al. 2012).

We have studied ρ Oph A from space and the ground in a variety of spectral lines and in the continuum. The first results, focussing on the dust properties and the gas-to-dust relationship, are presented in Paper I of this series (Liseau et al. 2015). The subregions of ρ Oph A that were observed with various instruments aboard *Herschel* (Pilbratt et al. 2010) are outlined in Fig. 1, superposed onto an image in the $C^{18}O$ (3–2) line; in this paper, we investigate further the complex physical and chemical interplay between the gas and the dust in ρ Oph A, and what their relation is with regard to star formation per se.

In Sect. 2, the observations and the reduction of the data are described. In Sect. 3, the spatially resolved low-(G_0/n) photon dominated region (PDR) is introduced. In Sect. 4 these data are compared with theoretical PDR models, and the O_2 formation in ρ Oph A and possible scenarios of observed protostellar mass infall are discussed. In Sect. 5 our main conclusions of this paper are summarized, and in Sect. 6 a synergy of the results and conclusions of Papers I and II are put into the wider context of star formation. Finally, our Odin mapping observations in the H_2O ($1_{10}-1_{01}$) line of ρ Oph A, B1, B2, C, D, E, and F are presented in Appendix A.

2. Observations and data reduction

2.1. H_2O, NH_3, and N_2H^+

The ρ Oph A cloud was observed in two H_2O lines with the heterodyne instrument for the far infrared (HIFI; de Graauw et al. 2010) on board the ESA spacecraft *Herschel* (Pilbratt et al. 2010) carrying a 3.5 m telescope. The 557 GHz data were acquired during OD 475, 1226, and 1231 in mixer band 1b and the 1670 GHz (179.5 μm) data on OD 1221 in band 6b. Data were taken simultaneously in the *H*- and *V*-polarizations using both the wide band spectrometer (WBS; accousto-optical) with 1.1 MHz resolution and the high resolution spectrometer (HRS; correlator) with 0.25 MHz resolution. The Band 1 receiver was tuned such that rotational transitions of ammonia and diazenylium, i.e. both the NH_3 (1_0-0_0) 572 GHz line and the N_2H^+ (6–5) 560 GHz transition, were also simultaneously admitted. The map and observational details for diazenylium can be found in Paper I.

For the programme GT2_rliseau_1, the mapping was done on the fly (OTF) with a reference position at (−10′, −10′) on OD 475, 1226, and 1231. At 557 GHz, the map size was $8' \times 6\overset{\prime}{.}5$ with samplings in 16″ steps. At 1670 GHz (OD 1221), the map was $2\overset{\prime}{.}5 \times 1'$ with a sampling rate of 20″. The observing times were 7 and 3 h, respectively. All data have been reduced with the HIFI pipeline HIPE version 14.1.0. Instrument characteristics are provided by Roelfsema et al. (2012) and some of the observational parameters can be found in Table 1.

The NH_3 (1_0-0_0) and N_2H^+ (6–5) lines were simultaneously observed with the H_2O ($1_{10}-1_{01}$) transition. These rectangular

Table 1. Instrumental reference: *Herschel*.

Species and Transition	Frequency ν_0 (GHz)	Wavelength λ_0 (μm)	Energy $E_{\rm up}/k$ (K)	Beam width *HPBW* ($''$)	Main beam efficiency $\eta_{\rm mb}$
PACS					*a*
[O I] ($^3P_1$–$^3P_2$)	4744.738586	63	228	7	0.73
($^3P_0$–$^3P_1$)	2060.052199	145	326	12	0.54
H_2O ($2_{12}-1_{01}$)	1669.904775	179	114	13	0.30
HIFI					*b*
H_2O ($2_{12}-1_{01}$)	1669.904775	179	114	13	0.55
$C^{17}O$ (7–6)	786.2808166	381	151	26	0.60
O_2 (5_4-3_4)	773.839512	388	61	27	0.60
^{13}CO (7–6)	771.184125	389	148	27	0.60
NH_3 (1_0-0_0)	572.498160	524	27	36	0.62
N_2H^+ (6–5)	558.957500	536	94	37	0.62
H_2O ($1_{10}-1_{01}$)	556.9359877	538	61	37	0.62
CS (10–9)	489.7509210	612	129	42	0.62
O_2 (3_3-1_2)	487.249264	616	26	44	0.62

Notes. [a] PCalSpectrometer_Beam_v6: for 62, 45 and 168/187 μm spatial averages are shown. [b] Mueller et al. (2014), Release Note #1, HIFI-ICC-RP-2014-001, v1.1.

maps were all observed at an angle of 55° with respect to the equatorial coordinate system and had to be rotated for proper alignment. The rotation and regridding of the data can be found in Bjerkeli et al. (2012) and in Paper I.

2.2. O_2

Following up on our initial O_2 observations with HIFI (Liseau et al. 2012), we obtained data in the O_2 (3_3-1_2) 487 GHz line towards 12 new positions on OD 1357, 1358, 1367, and 1371 (OT2_rliseau_2, 38.5 h integration time). In addition, the O_2 (5_4-3_4) 773 GHz line in HIFI Band 2 was observed towards HH 313 A, an optically visible shocked region of the VLA 1623 outflow (8.5 h integration on OD 1384). The reduction of these new data also followed the procedures outlined in the 2012 paper.

All in all, in ρ Oph A we observed O_2 487 GHz towards 15 positions and O_2 773 GHz towards five highly oversampled positions, each corresponding in size to that of the 487 GHz data. The 773 GHz *Herschel* beam was $27''$ and the grid spacing $10''$.

2.3. O I

Observations of the fine structure components of O I at 63 μm ($^3P_1$–$^3P_2$) and 145 μm ($^3P_0$–$^3P_1$) of the inverted ground state with the ISO-LWS (Long Wavelength Spectrometer, Clegg et al. 1996) towards the VLA 1623 outflow have been presented earlier by Liseau & Justtanont (2009). On OD 1202, the Photodetector Array Camera and Spectrometer (PACS, Poglitsch et al. 2010) was used to map the fine structure line emission north of the outflow (see Fig. 1) as part of the programme GT2_rliseau_2 and with an observing time of 2 h 16 min. The map consists of 3×4 PACS rasters separated by $38''$. An individual PACS raster covers $47'' \times 47''$ and is composed of 5×5 spaxels (spatial pixels), providing a spatial sampling of $9\farcs4$ per spaxel. At 63 μm, the spectral resolution is about 3500, and at 145 μm ~ 1000, corresponding roughly to 100 and 300 km s^{-1}, respectively. The lines in ρ Oph A are therefore expected to be unresolved, except perhaps towards the outflow.

The observing mode was unchopped grating scan and a position about $1\fdg5$ NE of the map was used as a reference. To estimate the absolute accuracy of the fluxes we compared data from one map position with those that we previously obtained with the ISO-LWS (e.g. Liseau & Justtanont 2009). However, we refer here to re-reduced data using the final version of the pipeline (OLP 10). The LWS line and continuum fluxes were both measured using two methods: the default point-source calibration and by exploiting extended source corrections. To compare the PACS measurements with those with the LWS, the PACS data were convolved with a flattened top Gaussian beam (Larsson et al. 2000) and with a pure equivalent aperture measurement. The results show that these two different methods lead to intra-instrumental agreement within 10–30%.

2.4. H_2 and polycyclic acromatic hydrocarbons

Towards ρ Oph A, the infrared space observatory (ISO) archive contains three frames of spectrophotometric data using the ISOCAM CVF (Circular Variable Filter; Cesarsky et al. 1996). For one frame, the pixel field of view (FOV) is $300''$ and it images the region around the star GSS 30. The other two, with a pixel FOV of $600''$, cover the VLA 1623 outflow (Liseau & Justtanont 2009) and the PDR of S 1, respectively. Together, these two frames cover most of the ρ Oph A region. In addition, *Spitzer* data of the NW part of the VLA 1623 outflow have been presented by Neufeld et al. (2009).

Towards the S 1 PDR region, PAH emission totally dominates the spectrum over the wavelength range of the ISO-CVF (see also Justtanont et al. 2008). However, three pure rotational H_2 lines, S(2), S(3), and S(5), could also be extracted. The S(5) line at 6.9 μm is relatively unaffected by other spectral features, while the S(2) 12.3 μm line is blended with a PAH feature and the S(3) 9.3 μm line is situated inside the deep silicate absorption. Consequently, the fluxes for these two lines are more uncertain. The observations and procedures to reduce the CVF data

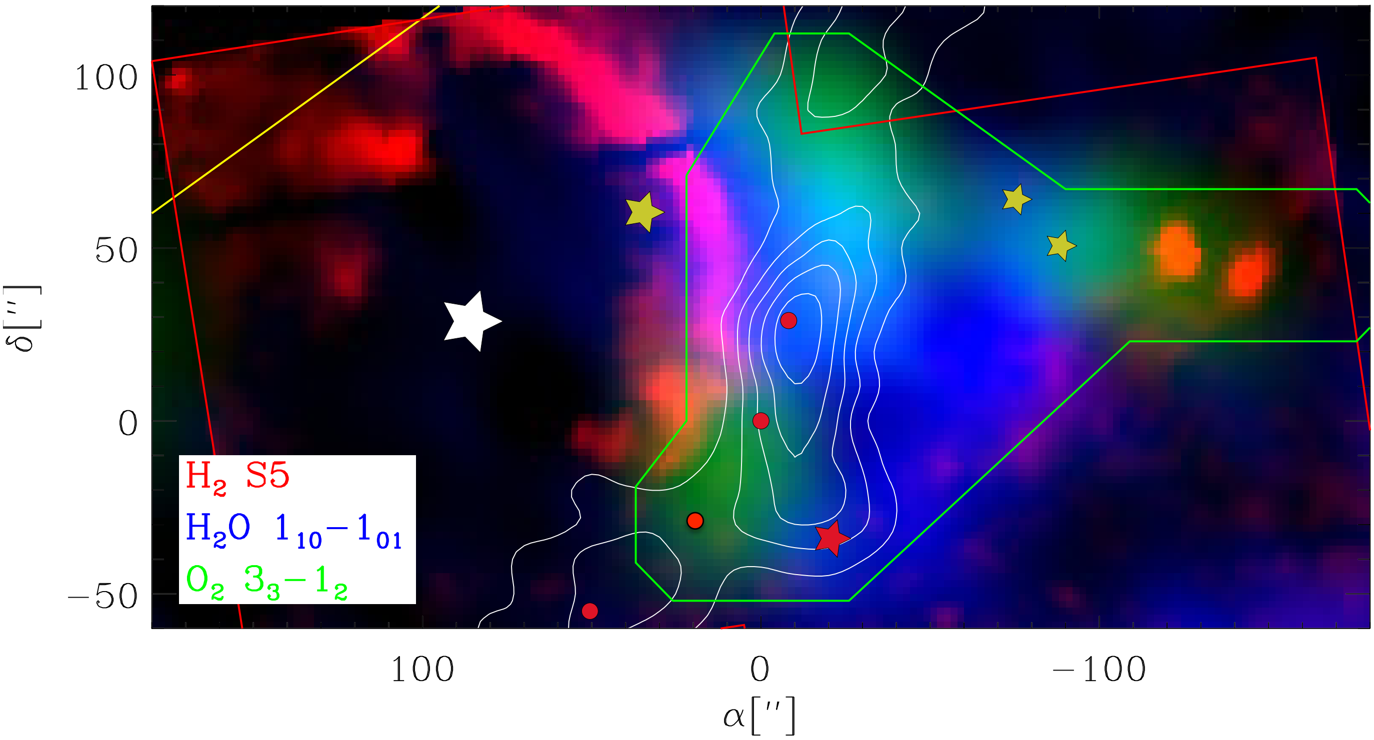

Fig. 2. Observed layers of the edge-on PDR in ρ Oph A. *From left to right*: H_2 6.9 μm, O_2 487 GHz, and H_2O 557 GHz are shown in red, green, and blue, respectively. Symbols are as in Fig. 1 and the region of H_2 observations is shown by the partial red polygon. The H_2 sources near (–100, 50) are gas shocked by HH-flows (see also Liseau & Justtanont 2009), and faint H_2 emission can also be seen from the VLA 1623 outflow. The white contours outline the integrated N_2H^+ (3–2) emission, indicating the presence of dense gas above 10^6 cm^{-3} (Liseau et al. 2015, Paper I).

are described in detail by Liseau & Justtanont (2009). There, numerical model fits to the spectral PAH features were used to estimate the fluxes also of other H_2 lines. Comparing these results with the present ones, where possible, demonstrates excellent agreement.

2.5. CS and CO

CS (10–9) data were obtained simultaneously with the O_2 487 GHz maps with HIFI. Complementary data had previously been collected with the 15 m Swedish ESO Submillimetre Telescope (SEST, Booth et al. 1989) in the CS transitions of (2–1), (3–2), and (5–4), in addition to pointed observations in the isotopologues $C^{34}S$ and $^{13}C^{34}S$ (see Appendix C).

Simultaneously with the O_2 773 GHz line, 50″ × 50″ maps at 10″ sampling of ^{13}CO (7–6) and $C^{17}O$ (7–6) were obtained (see Fig. 8 below).

3. Results: A spatially resolved PDR

The mapping in atomic and molecular line emission revealed a spatially resolved PDR, seen from the side (“edge-on”).

3.1. Hydrogen, H_2

As can be seen in Fig. 4, the H_2 S(2) emission outlines a clear spherical shell structure of warm PDR gas around the stellar object S 1. In the figure this structure is also seen in the S(3) and S(5) lines, but at a slightly more fragmented level. This spherical structure motivates the radial averaging of the H_2 fluxes and these are plotted in the lower rightmost frame of Fig. 4, together with a model fit using the Meudon PDR code[1] (Le Petit et al. 2006, see below). The formation of H_2 on grain surfaces is taken into account (Le Petit et al. 2009; Le Bourlot et al. 2012).

The observed data are consistent with gas at a temperature of about 10^3 K that has a total column density of a few times 10^{19} cm^{-2}, values that are identical to those determined by Liseau & Justtanont (2009) towards the VLA 1623 outflow, and where an H_2 ortho-to-para ratio of 2 was derived.

3.2. Oxygen: O I and O_2

3.2.1. Atomic oxygen, O I

As in the H_2 image, the VLA 1623 outflow is also seen in the upper part of the leftmost panel of Fig. 4, showing the distribution of the fine structure line emission of [O I] ($^3P_1$–$^3P_2$) 63 μm. In the upper middle panel, the distribution of the ($^3P_0$–$^3P_1$) 145 μm line, originating from a higher upper level[2], is also shown. These atomic fine structure lines mark very clearly the boundary seen in H_2, but also show significant emission throughout the entire molecular cavity around the stellar object S 1. As seen from the centre to the edge of this region, the extinction is limited to $A_V \le 3 \times 10^{-3}$ magnitudes, equivalent to a hydrogen column density of 4.2×10^{18} cm^{-2} (see Paper I). For a solar oxygen abundance (5×10^{-4}; Asplund et al. 2009) we would expect an [O I] 63 μm flux of about 4×10^{-12} erg cm^{-2} s^{-1}. Observed flux levels are lower than 6×10^{-13} erg cm^{-2} s^{-1}. In a low-density medium and at temperatures of some 10^3 K, essentially all O^0 atoms are in the

---

[1] Unless explicitly noted, we are using standard values of the code.

[2] The upper level energy E_0/k of the 145 μm line is 326 K above ground, and for the 63 μm transition, $E_1/k = 228$ K.

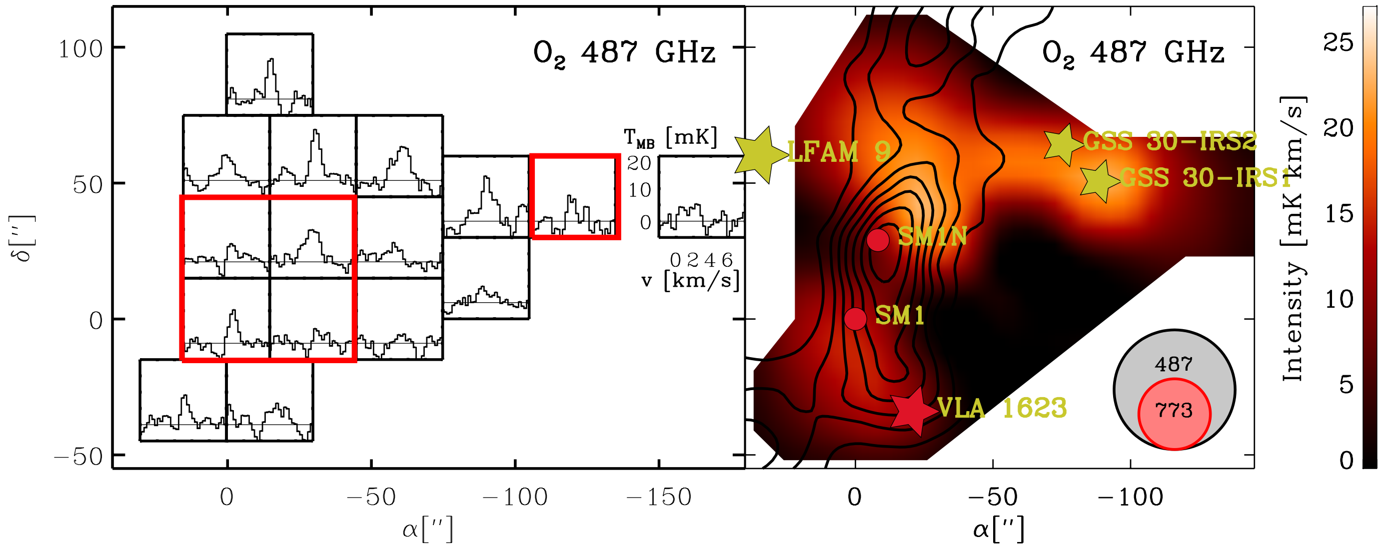

Fig. 3. *Left*: map of ρ Oph A in the O_2 (3_3−1_2) 487 GHz line with HIFI. At the positions of the red frames oversampled O_2 (5_4−3_4) 773 GHz spectra were obtained. Scales in km s^{-1} and mK are indicated in the spectrum of the off-position (westernmost frame). *Right*: contour-colour map of the data shown in *the left panel*. The colour bar for the integrated intensity in mK km s^{-1} is shown to the *right*. The contours outline integrated N_2H^+ (3–2) emission.

$^3P_2$ ground state. This observed flux deficiency could therefore indicate that the 63 μm line is self-absorbed. This hypothesis can be tested by a comparison with the observed 145 μm transition.

The upper right panel in Fig. 4 displays the line flux ratio $F_{63\,\mu\mathrm{m}}/F_{145\,\mu\mathrm{m}}$. In PDRs, observed values are generally around 10 to 20 (Hollenbach & Tielens 1999). It is therefore remarkable that some regions show ratios ten times lower, and even lower than unity. The region in the southeast where this occurs, i.e. N 6, is otherwise conspicuous only in N_2H^+ emission (Di Francesco et al. 2004, and Paper I).

Line ratios of the magnitude observed here are characteristic of gas that is neither optically thin nor in thermodynamic equilibrium (e.g. Liseau et al. 2006; Canning et al. 2016). Oxygen fine structure lines from cold gas ($\lesssim$20 K), which are optically thick in both ground state transitions, can show ratios below unity. A gas kinetic temperature of 17 K in this particular region was recently determined in Paper I. However, the N 6 column density, $N(H_2) = 2 \times 10^{23}$ cm^{-2}, is too low by a factor of 300 for the $^3P_{0-1}$ 145 μm optical depth to reach unity (see Liseau et al. 2006) and must therefore be dismissed as an explanation. Instead, as advocated by these authors, a cold foreground cloud that absorbs much of the $^3P_{1-2}$ 63 μm radiation but leaves the higher level $^3P_{0-1}$ 145 μm line unaffected appears to be the only viable alternative to explain the very small 63 μm to 145 μm flux ratios of N 6.

3.2.2. Molecular oxygen, O_2

In Fig. 4 it can be seen that the atomic oxygen, O I, appears to be penetrating quite deeply into the dense parts of the dark core ρ Oph A, outlined by the contours of the N_2H^+ emission. It feeds the O_2 production region (Fig. 3) with atomic oxygen. There, the molecular oxygen is produced in the gas phase, with additional contribution from the ice-crusted dust grains (Hollenbach et al. 2009). The models of Melnick & Kaufman (2015) for Orion A, which invoke shock chemistry, do not likely apply to ρ Oph A as the O_2 emission regions and the outflow/HH-shocks are spatially well separated. In ρ Oph, these shocks enhance the H_2O abundance, but not that of O_2.

Unfortunately, our O_2 map is not complete and maximum emission occurs near the edge of the map. To remedy this, complementary observations would be required. However, after the decommissioning of *Herschel*, there is no other facility available or planned any time soon. The factor of two higher intensity at the local O_2 emission maximum is likely an effect of the increased temperature (25 K) rather than a higher column density of O_2 molecules.

3.3. Water, H_2O

3.3.1. Spectral components of the line profiles

The emission due to water is seen essentially everywhere in the molecular core ρ Oph A, except in the easternmost parts towards the early-type stellar object S 1, where the water molecules have been destroyed by the radiation from the B-star.

The lines of the two ground state transitions[3] of ortho-H_2O have a different appearance. For the (1_{10}−1_{01}) 557 GHz line, the spectral profiles exhibit a complex structure with emission peaks, deep central absorptions, and extended wings. Maps of these features reveal that these dominate different parts of the cloud core (Fig. 5). That is, the wings outline the bipolar, jet-like molecular outflow from the protostellar object VLA 1623 (Bjerkeli et al. 2012), whereas the line core is most prominent in the denser parts of ρ Oph A where $n(H_2) \geq 3 \times 10^6$ cm^{-3} (Paper I). Comparing the 557 GHz HIFI data with those that were obtained earlier with Odin (see Appendix A) and also SWAS[4] shows that these components of the line shape are excellently reproduced by different instruments in independent observations (Fig. A.2).

The HIFI observation of the higher excitation line H_2O (2_{12}−1_{01}) 1670 GHz is a completely new result, but with its three times smaller beam the map is not as extended as that for the 557 GHz line. However, our strip map of the dense core region of ρ Oph A (Fig. 1) is still useful for a comparison of the two

---

[3] For the lowest rotational levels, an energy diagram can be found in van Dishoeck et al. (2011).

[4] Submillimeter Wave Astronomy Satellite (SWAS; Melnick et al. 2000).

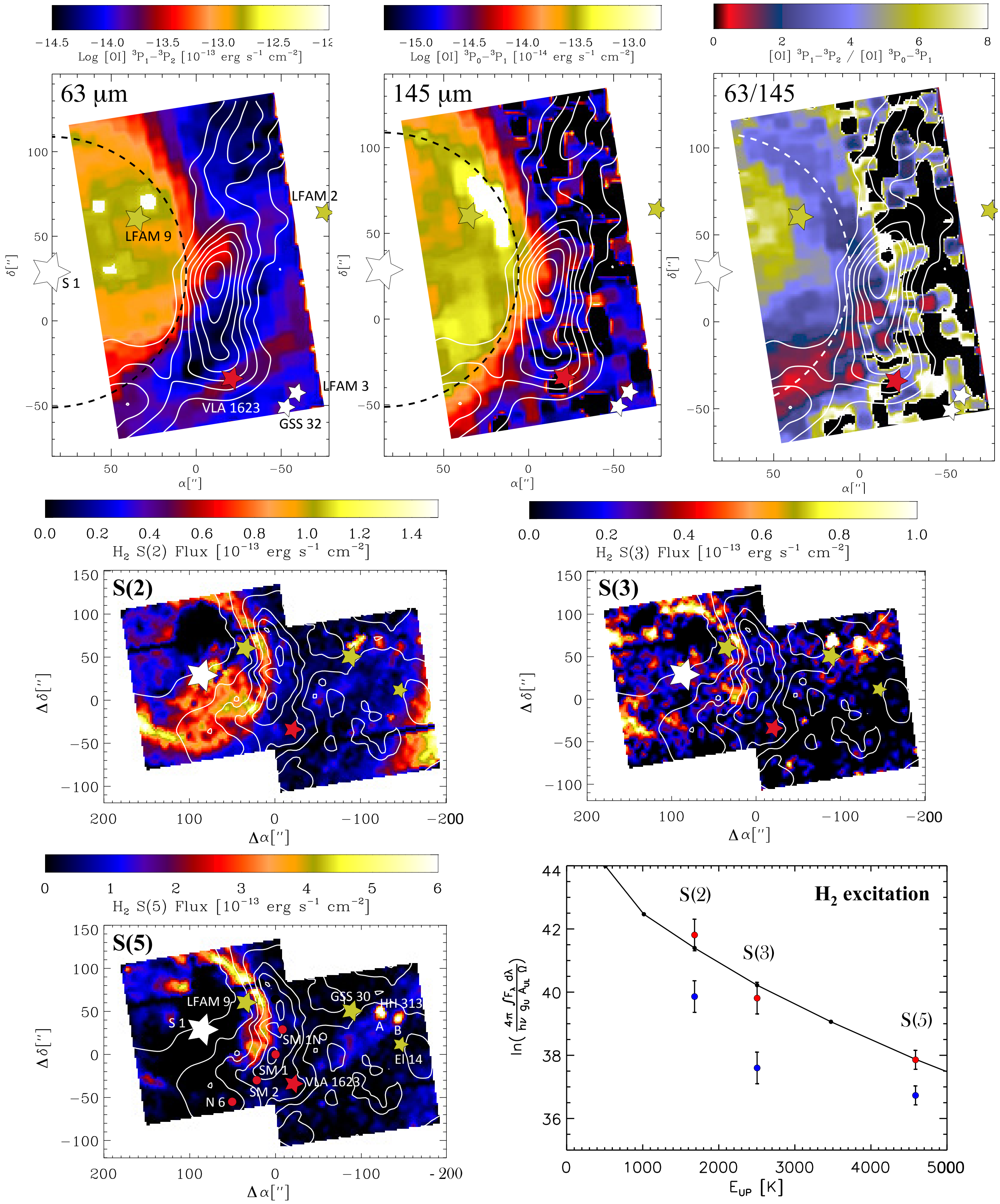

Fig. 4. *Upper panels*: (*from left to right*) Distribution of the emission in [O I] 63 μm, [O I] 145 μm, and the ratio of their intensities I([O I] 63 μm)/I([O I] 145 μm). The illuminating source, S 1, is depicted as a white star on the left side of the frames, being at the centre of the dashed circles. The white contours outline integrated N_2H^+ (3–2) emission. *Lower panels*: distribution of the S(2), S(3), and S(5) pure rotational lines of H_2 are shown by the coloured maps, with the fluxes given by the scale bars. These data were obtained with the ISOCAM-CVF. The white contours and the symbols are as in Fig. 1. The graph shows the fit with the Meudon PDR code (Le Petit et al. 2006, red dots) to the dereddened observations for $A_V = 6$ mag. Blue data points are the observed values. Other H_2 lines, i.e. S(1) and S(4), are also filled in and shown as black dots.

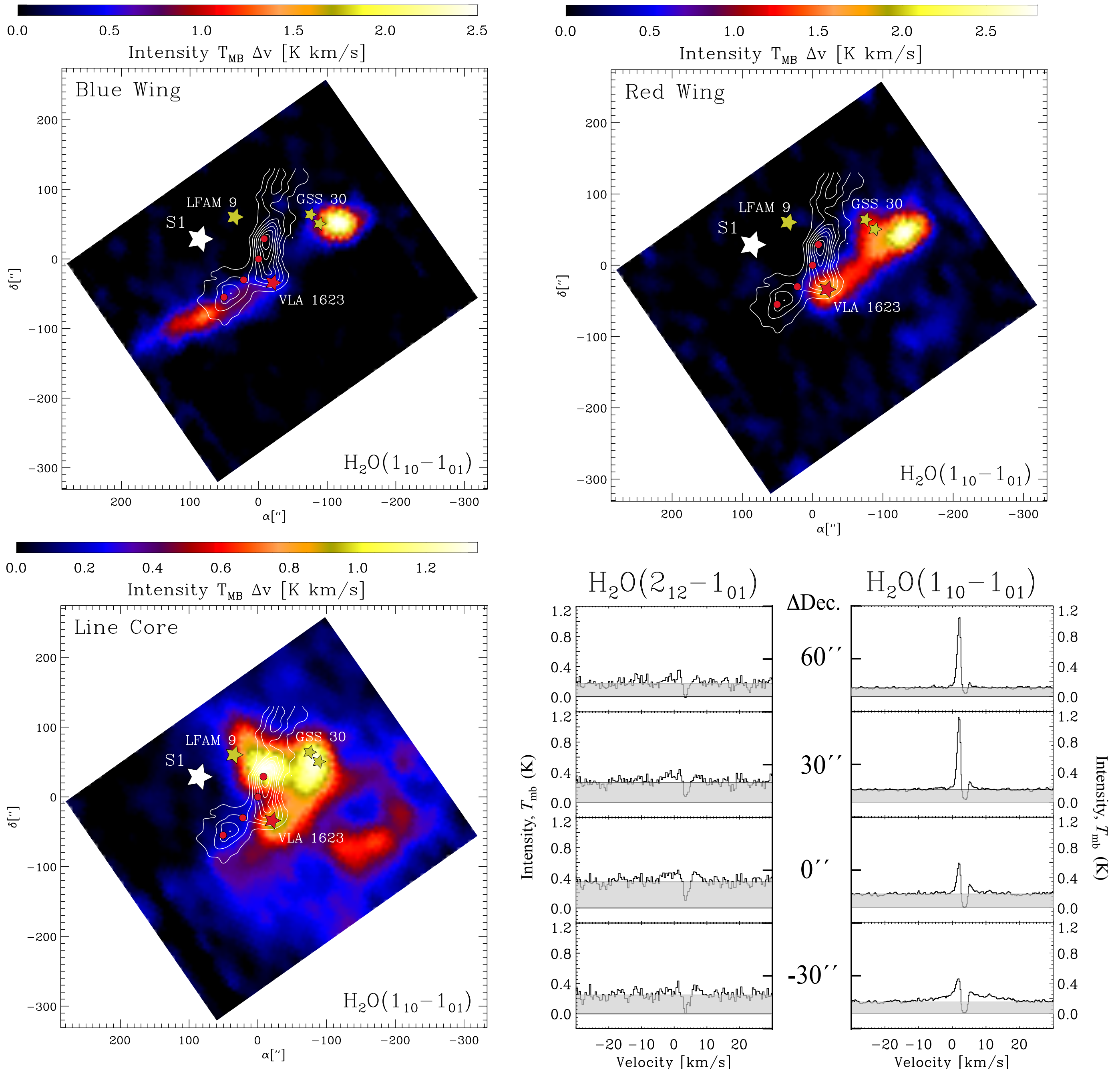

Fig. 5. *Upper and lower left*: HIFI maps of the kinematic components of the ortho-H_2O 557 GHz line referring to the VLA 1623 outflow, labelled “Blue Wing” and “Red Wing”, respectively, and that of the quiescent gas of the “Line Core”. Specifically, the integrations of the intensity, $\int T\,d\upsilon$, were over $[-30, -2[$ km s^{-1} for the blue wing and over $] + 5, +40]$ km s^{-1} for the red wing. The line core is bounded within $[-2, +2]$ km s^{-1}. A deep absorption feature is observed in the range $\upsilon_{\rm LSR} = [+2, +5[$ km s^{-1}. The contours outline observed N_2H^+ (3–2) emission. *Lower right*: HIFI north-south strip map about the Right Ascension offset $\Delta\alpha = 0''$ in H_2O 1670 GHz (*left*) and 557 GHz (*right*), see also Fig. 1. The declination offsets (ΔDec) are indicated between the frames. Both data sets were convolved to a beam size of 38″. To compensate for the observation in double sideband mode the continuum intensity, shown in shaded grey, has been divided by a factor of two.

line profiles (see Fig. 5). The 557 GHz line displays several components, whereas the 1670 GHz line is mostly in absorption with weak wing emission towards the dark cores SM 1 and SM 1N. This may seem surprising, as these positions are not anywhere near the strong outflow from VLA 1623 (Fig. 5), but could be due to the weak CO outflows of Kamazaki et al. (2003).

The most significant part of the line profile, though, is the deep absorption feature, reaching down to close the zero level. The same depth is also seen in the $(1_{10}\text{–}1_{01})$ line, where the signal-to-noise (S/N) is significantly higher. There, however, the emission core varies appreciably in intensity with position. This is not an effect caused by a foreground absorber drifting over the cloud, thereby changing the strength of the emission peak, because the centre of the absorption dip in both lines is completely stable with respect to the systemic Velocity Standard of Rest ($\upsilon_{\rm LSR}$).

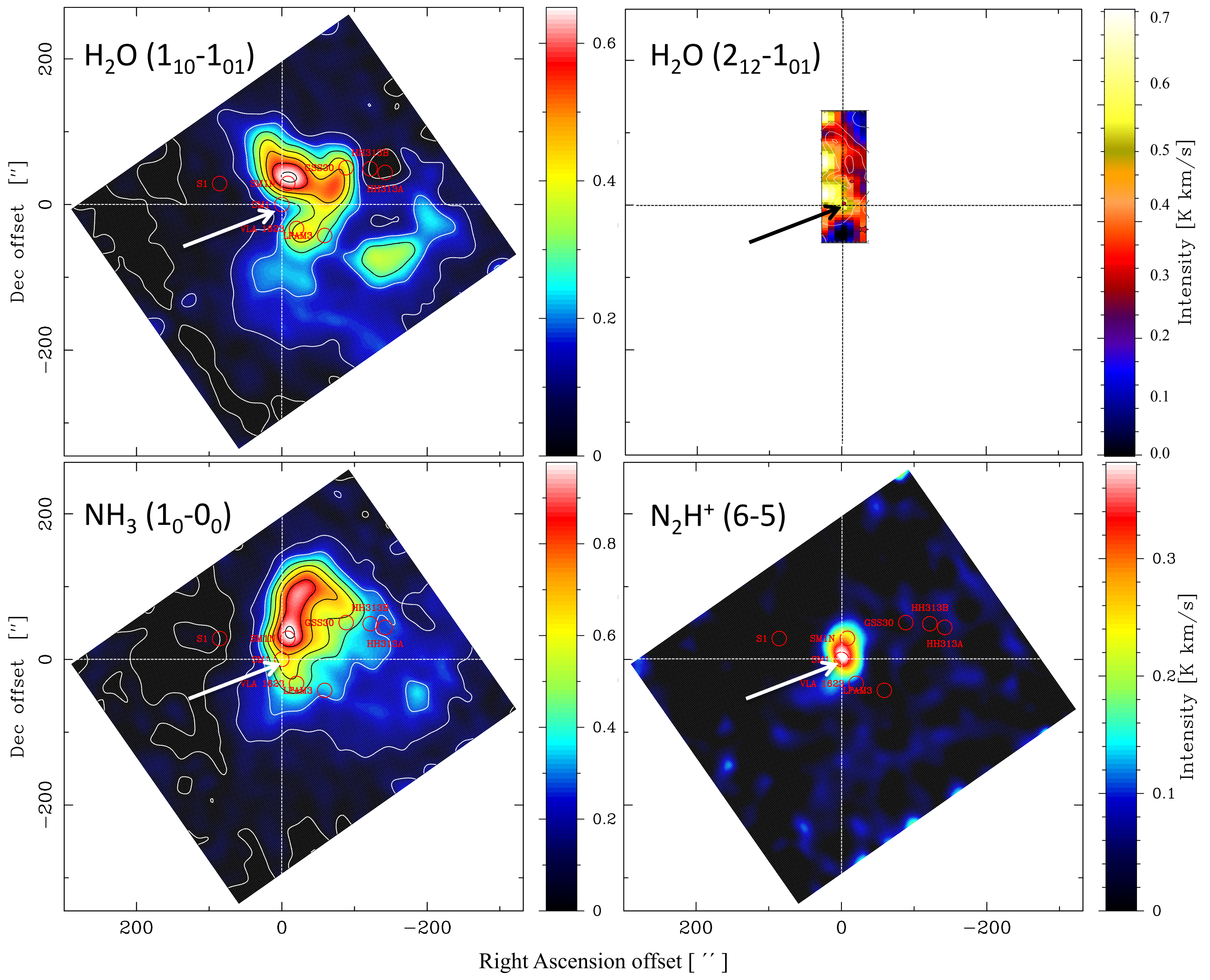

Fig. 6. *Herschel*-HIFI maps of integrated water, ammonia, and diazenylium emission. The scale bar to the right of each frame is in K km s^{-1} and the arrows all point to the location of the dark core SM 1 at the crosshair. Neither NH_3 nor H_2O peaks there, but N_2H^+ does. The maps of the line spectra of N_2H^+ (3–2) and (6–5) are presented in Paper I.

3.4. Ammonia, NH_3

The spatial distribution of the NH_3 (1_0–0_0) line is similar to that of H_2O (1_{10}–1_{01}), both being of the ortho flavour. As for water, ammonia peaks close to SM 1N. A clear difference is displayed by deuterated species, which all peak at the SM 1 position. For instance, formaldehyde has its emission maximum towards SM 1N, whereas its doubly deuterated form peaks towards SM 1 (Bergman et al. 2011b), i.e. D_2CO has essentially vanished towards SM 1N where the H_2CO emission is strongest. This difference may have its explanation in the fact that temperatures are lower at SM 1 (Paper I), promoting the exothermic process of molecular deuteration. However, Friesen et al. (2014) detected H_2D^+ towards SM 1N, but not towards SM 1.

The ground state lines of both H_2O and NH_3 have double-peaked line profiles. However, a remarkable difference between the ammonia and water lines are the high-velocity wings that are entirely absent in the ammonia data (Fig. 12). Consequently, low-amplitude velocity fields like those due to gravitational infall are potentially better traced in the NH_3 lines.

3.5. Carbon monoxide, CO

In an adjacent shell, next to H_2, low-*J* CO is distributed along a dense ridge that is broken up into several high-density clumps, of which SM 1 and SM 1N are the most conspicuous ones (Fig. 1).

Profile maps of ^{13}CO (7–6) and C^{17}O (7–6) have been secured simultaneously with the observations of O_2 (5_4–3_4) 773 GHz as prime. The positions are identified in Fig. 3 by the red rectangles. The profiles are fit by a two-component model, where Gaussians were fitted to the observations. Westward of the ridge, the isotopologues of CO decline rapidly.

3.6. Methylidine, CH^+, and ethynyl, C_2H

At the very edge of the PDR-interface, the (J = 2–1) line of the cation CH^+ has been mapped simultaneously with the H_2O (2_{12}–1_{01}) line at 179.5 μm. In the left frame of Fig. 9, it can be clearly seen that the emission arises in front of the cores SM 1N, SM 1, and SM 2 (red dots from north to south) as seen from the B star S 1.

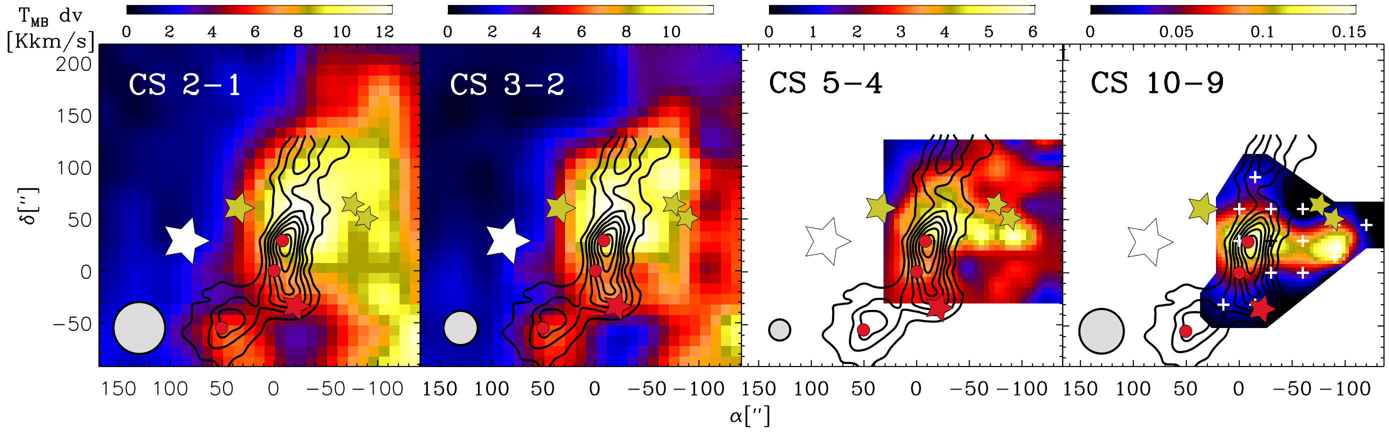

Fig. 7. Maps of integrated CS line intensity, $\int T_{\rm mb}\,{\rm d}\upsilon$, of CS (2–1), (3–2), (5–4), and (10–9). Symbols are as in Fig. 1 and the half-power widths of the telescope beams are shown as grey circles in the lower left corners (see Tables 1 and C.1). The contours show the distribution of N_2H^+, as traced by its (J = 3–2) line (Paper I).

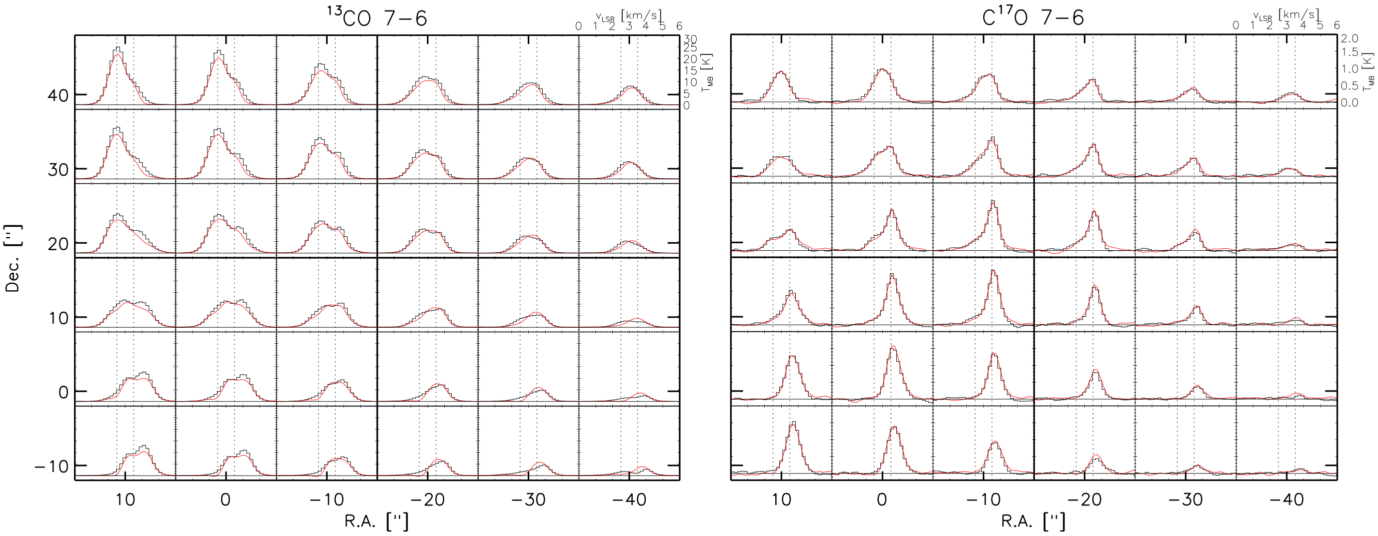

Fig. 8. Oversampled maps in ^{13}CO (7–6) (*left*) and C^{17}O (7–6) (*right*) with the 27″ beam of *Herschel*. The $\upsilon_{\rm LSR}$ and $T_{\rm mb}$ scales are indicated in the upper right corners. The dashed vertical lines, at LSR velocities of 2.5 km s^{-1} and 3.5 km s^{-1}, respectively, identify two radial velocity components of the fitted Gaussians, shown by the smooth red curves, whereas the observations are shown as histograms.

In contrast, the neutral C_2H radical is detected further in and closer to the cores, where the UV penetration into the cloud has diminished due to the increased extinction by the dust (Fig. 9, right-hand panel).

3.7. Carbon sulfide, CS

The CS maps, up to (J = 5–4), were obtained at the SEST (Appendix C) and the (J = 10–9) data with HIFI aboard *Herschel*. These maps indicate, following the excitation gradient of the PDR, that CS appears behind CO and not predominantly in the densest parts of the cloud core.

4. Discussion

4.1. The ρ Oph A – PDR

For the stellar parameters given in Table 5 of Paper I, and assuming solar elemental abundances, we use ATLAS 9 model atmospheres for the energy distribution of the stars (Castelli & Kurucz 2004). At 0.05 pc from S 1, the FUV field[5] amounts to roughly 5000 in terms of G_0, whereas the western side is illuminated by a $G_0 \sim 100$ field from HD 147889.

The extinction towards ρ Oph A is well described by a law with $R_{\rm V} = 5.5$, so that the gas-dust relation reads $N({\rm H\,I} + {\rm H}_2) = N({\rm H\,I}) + 2\,N({\rm H}_2) = 1.4 \times 10^{21}\,A_V\,{\rm cm}^{-2}$ (Bohlin et al. 1978, see also Paper I).

4.2. The physical conditions in ρ Oph A

4.2.1. A gaseous sphere around S 1

At distances greater than 3×10^{16} cm from the centrally positioned S 1, radiation pressure on the hydrogen gas is not very important. Due to the efficient braking by the 600 to 10^3 cm^{-3} gas (seen in [O I] throughout this region, Fig. 4), radiation pressure in the Lyman lines can result in terminal velocities of only

---

[5] For a definition of G_0, see e.g. Hollenbach & Tielens (1999).

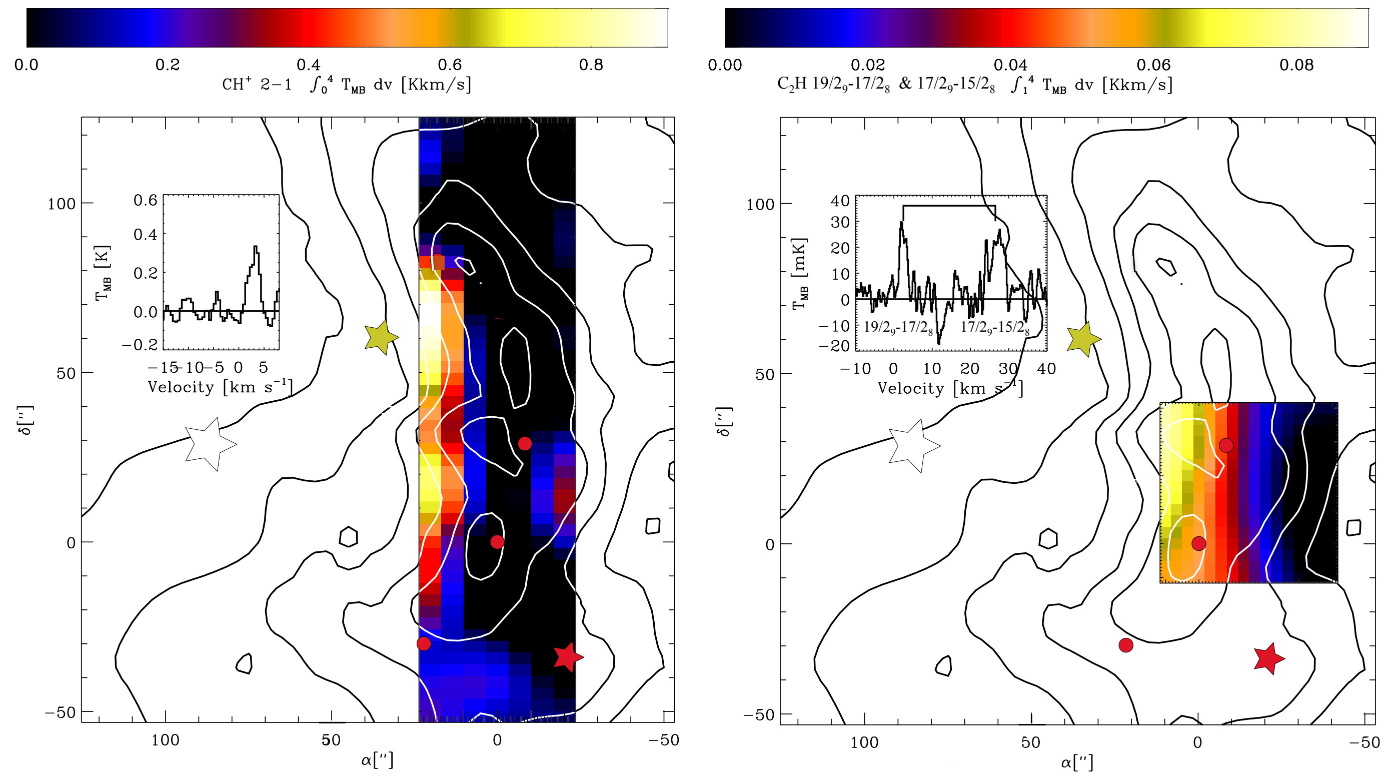

Fig. 9. *Left*: HIFI-map of the 1.67 THz methylidine line, CH^+ (2–1), obtained simultaneously with H_2O ($2_{12}-1_{01}$). *Right*: small map of the emission in ethynyl, C_2H ($17/2_9-15/2_8$, $19/2_9-17/2_8$) 786 GHz, observed together with O_2 (5_4-3_4) 773 GHz. The contours and symbols are as in Fig. 1.

a few times 10^{-2} km s^{-1} at the 0.05 pc interface[6]. This is much smaller than the turbulent speed of a few times 10^{-1} km s^{-1} in the cloud core and therefore has little impact on its dynamics.

Without any significant dynamical pressure gradients, the nearly perfectly spherical shape of this region is kept in place by a delicate pressure balance, where the higher temperature of the H region is offset by the higher density of the molecular core, i.e. $P_{\rm H}/P_{\rm H_2} \sim 600\,{\rm K} \times 3 \times 10^4\,{\rm cm}^{-3}/10\,{\rm K} \times 2 \times 10^6\,{\rm cm}^{-3}$. In high-($G_0/n$) PDRs the situation is different, where an H II region drives an ionization front into the molecular cloud (e.g. Tielens 2005). A clumpy structure would further alter both molecule formation depths and, in particular, the radiative transfer.

4.2.2. Abundant O_2 production in ρ Oph A

Of considerable interest is to understand the formation history of O_2 in ρ Oph A as this molecule, in spite of numerous attempts (Goldsmith et al. 2000, 2002; Pagani et al. 2003; Yıldız et al. 2013; Sandqvist et al. 2015; Wirström et al. 2016), has hardly been found anywhere else outside the solar system. Taking into account new lab results for the oxygen binding energy on dust grains (He et al. 2015), Taquet et al. (2016) recently discussed a number of formation scenarios and argued in favour of a particular one that could fit the physical conditions in ρ Oph A.

Taquet et al. (2016) suggested that the high abundance of O_2 seen in the gaseous comae of two solar system comets, with $X(O_2)/X(H_2O) = 0.01$–0.1 (Bieler et al. 2015; Rubin et al. 2015), points towards a primordial origin, i.e. that this O_2 was initially produced in the protosolar cloud core and subsequently transported through the viscous protoplanetary disc to its inner regions. It is argued that chemistry on icy dust grains would produce observed levels of related species, i.e., $X(H_2O_2)/X(O_2)$ and $X(HO_2)/X(O_2)$, see Bergman et al. (2011b) and Parise et al. (2012), respectively, and with the accompanying theoretical chemistry models presented by Du et al. (2012a,b).

However, we find it very difficult to reconcile the comet results for O_2 and H_2O with our abundance determinations for ρ Oph A, i.e. $X(O_2) = 5 \times 10^{-8}$ (Larsson et al. 2007; Liseau et al. 2012, this paper) and $X(H_2O) = 5 \times 10^{-9}$ (see Sect. 4.3.2), hence $X(O_2)/X(H_2O) = 10$.

In a model specifically designed for ρ Oph A, Taquet et al. (2016, see their Fig. 6) find that $X(O_2)/X(H_2O) > 1$ during the time of about 5000–30 000 yr on their chemical clock, with a free-fall time of 16 000 yr (see below) falling right into this interval. If this chemical model is basically correct (there might be issues with their HO_2 and H_2O_2 abundances), the data would suggest the dense clumps in ρ Oph A to be (chemically) very young indeed. As discussed by Liseau et al. (2012), the relative brevity of the period of abundant O_2 in the gas phase would readily explain the elusiveness of this molecule in the interstellar medium.

4.3. *Theoretical models of infall: H_2O*

The HIFI instrument aboard *Herschel* is based on the heterodyne technique that implies high spectral resolution, $\nu/\Delta\nu > 10^6$. At the operating frequencies of HIFI, radial velocity resolutions are fractions of a km s^{-1}, sufficient to spectrally resolve narrow molecular lines that originate in the cold interstellar medium.

4.3.1. Line profiles: H_2O ($1_{11}-1_{10}$)

Due to their expected high optical depths (>100), the ground state lines of water are particularly suited as tracers of protostellar infall, as these large optical depths lead to large

---

[6] These computations are based on an ATLAS 9 model atmosphere for $T_{\rm eff} = 17\,000$ K, $\log g = 4.0$, [M/H] = 0.0 (Castelli & Kurucz 2004).

contrasts between receding and approaching emission. The high optical depths, in combination with the complex system of its many energy levels of the water molecule, imply however that the radiative transfer is difficult and the proper computation is therefore often avoided. A widely used method is to fit the observed profiles, essentially "perfectly", with multi-component Gaussian functions; however, this procedure does not appropriately recover the physics and so we turn to other options.

We compute the line profiles from a physical model and account for the radiative transfer using an Accelerated Lambda Iteration (ALI) code; at these high optical depths other possibilities such as Monte Carlo methods frequently run into conversion problems. The benchmarking of the ALI code has been described by Maercker et al. (2008). In the present work, the collisional rate constants of Faure et al. (2007) are used.

4.3.2. Profiles of the infall centre

The observed 557 GHz line profile, with its blue-red asymmetry and deep central absorption, is highly reminiscent of theoretical profiles of spherical infall, i.e. from a protostar at the onset of gravitational collapse prior to observable disc formation (e.g. Ashby et al. 2000).

Because of its conceptual and computational simplicity (see e.g. Foster & Chevalier 1993), our protostar model is a Bonnor-Ebert sphere (BE, Bonnor 1957; Ebert 1957); based on observed criteria (Paper I), it is found to be gravitationally unstable (dimensionless mass[7] = 14.1, density contrast $\rho_0/\rho_{\rm out} = 29$). The critical BE mass is 1.04 $M_\odot$ within 3000 AU (25″), where the thermal pressure is 1.24×10^{-9} erg cm^{-3} ($T_{\rm out} = 30$ K, $n_{\rm out} = 3 \times 10^5$ cm^{-3}) and a free-fall time is 16 000 yr.

The line profiles to be compared to the observed ones are computed self-consistently, based on observation, and with the following ALI parameters: $T_{\rm kin}$ = 9 to 15 K, $\upsilon_{\rm turb}$ = 0.4 to 0.6 km s^{-1}, gas-to-dust mass ratio of 17.5, and a dust-β = 1.8. We found an average water abundance $X({\rm H_2O}) = 5 \times 10^{-9}$ that resulted in a central optical depth of 160 in the 557 GHz ground state line. This model correctly reproduces the observations of the spectra at the central position in both the ground-state lines of ortho-H_2O, i.e. the (1_{10}–1_{01}) 557 GHz and the (2_{12}–1_{01}) 1670 GHz transitions.

A subregion of our H_2O 557 GHz spectrum map is shown in Fig. 10, where the protostar SM 1N is shown by the red circle. Apparently, the basic feature of the characteristic line profile extends over a much larger region than that. A radial cut at half-beam spacing (about Nyquist sampled) is shown below the map, from which it is clear that the BE sphere model reproduces the observed line reasonably well at the infall centre. However, as one goes farther away from the centre, observation and model diverge increasingly (see the lower part of Fig. 10). Evidently, a one solar mass collapsing protostar alone cannot account for the observed widespread inverse P Cygni profiles. It should also be clear that the observation of the spectrum towards merely one single position will not be sufficient to provide unambiguous evidence of protostellar mass infall.

4.4. Theoretical models of infall: NH_3

4.4.1. Line profiles: NH_3 (1_0–0_0)

In contrast to the H_2O lines, the observed line profiles of NH_3 (1_0–0_0) are free from contaminating emission from the high-velocity gas in the outflow (Fig. 11). The ammonia ground-state line can therefore be assumed to be potentially better suited to tracing protostellar infall.

In Fig. 12b, an infall model whose physical parameters are similar to those for water has been computed for the NH_3 (1_0–0_0) line. The radiative transfer takes the overlap of the hyperfine structure (hfs) components explicitly into account. The highest optical depth of 240 is found at the frequency of the $F'-F = 2-1$ transition (see Appendix B), consistent with the observed absorption feature in the spectrum. Next to $F' - F = 2-1$ is the $F' - F = 1-1$ line that fits the observed red wing of the line. However, the theoretical emission peak is too low. This is in contrast to the blue peak that is well fitted in intensity, but there the wing is overestimated by the model. This appears to be a persistent feature of the computed profiles. Models that fit both the observed two-peak shape and the intensities have necessarily very high optical depths and the lines become broader.

We have also tried to fit a static BE configuration (Fig. 12a). As for the infall case, the ortho-NH_3 abundance is 1.5×10^{-8}, i.e. a factor of 35 higher than that found on the basis of our Odin observations with a 2′ beam (Liseau et al. 2003). Both the red wing and peak are well fit with this $\tau_0 = 260$ model; however, the blue peak intensity is much too low, and at the same time the blue wing is overestimated. The theoretical profile is too broad on the blue side, even though the turbulent speed is merely 0.3 km s^{-1}.

As for the H_2O lines, little compelling evidence for gravitational infall is provided by the ammonia line observations. Essentially perfect fits can be obtained by introducing two velocity components on an ad hoc basis (Fig. 12c). Good examples would be hypothetical components at $\upsilon_{\rm LSR} = +2.4$ and +4.1 km s^{-1}, and with $FWHM$ = 0.8 km s^{-1} and 0.9 km s^{-1}, respectively. However, on the basis of the analysis of N_2H^+ spectral line maps Liseau et al. (2015) found no evidence for different velocity components greater than 0.2 km s^{-1}. We therefore abandon the results from Gaussian profile fitting as unreliable indicators of the velocity fields in the source.

5. Conclusions

In the densest and coldest regions of ρ Oph A, the abundance ratio of O_2 to H_2O is of the order of ten. According to theoretical models of grain chemistry, $X({\rm O_2})/X({\rm H_2O}) > 1$ occurs only during brief periods of time, i.e. during intense O_2 production in dense cores. This would limit the (chemical) age of SM 1 to less than 30 000 yr and explain the elusiveness of O_2 outside the solar system.

Although the line shapes of the ground state line of H_2O (1_{10}–1_{01}) in ρ Oph A are textbook examples of protostellar infall, detailed modelling and radiative transfer calculations of the observed spatially extended emission makes this option unlikely. A similar conclusion is reached on the basis of accompanying NH_3 (1_0–0_0) observations.

Mapping the ρ Oph cores A, B1, B2, C, D, E, and F in the H_2O (1_{10}–1_{01}) line with Odin resulted in clear detections only in ρ Oph A. Upper limits are within 10 to 50 mK (rms).

6. Epilogue: star formation in ρ Oph A

ρ Oph A is a region of active low-mass star formation. It is special in some respects, but also shares common properties in others. Based on a large observational material, a few conclusions that should also be valid in a wider and general context can be drawn. Below we summarise our findings and combine the results of Papers I and II.

---

[7] $m = (4\pi\rho_0/\rho_{\rm out})^{-1/2}\,(\xi^2\,{\rm d}\psi/{\rm d}\xi)_{\xi_0}$, where ψ and ξ are the dimensionless gravitational potential and the radial variable in the Lane-Emden equation, respectively.

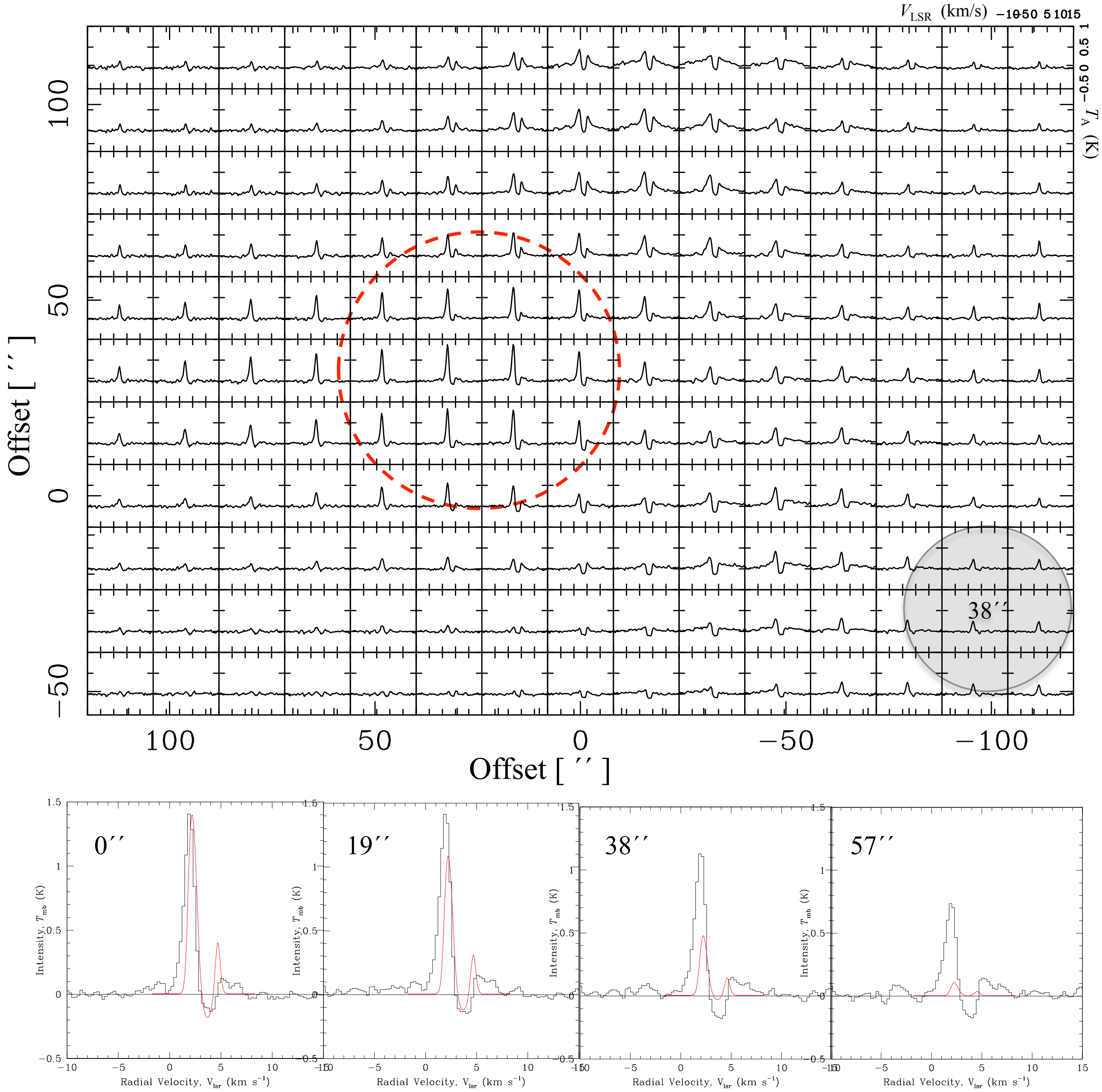

Fig. 10. *Upper*: subregion of the observed 557 GHz H_2O map of ρ Oph A. The scales of $\upsilon_{\rm LSR}$ and $T_{\rm A}$ are shown in *the upper right corner*. The *Herschel* beam at FWHM is indicated in the lower right corner (38″, grey). The red circle shows the size of the Bonnor-Ebert sphere model of SM 1N discussed in the text. *Lower*: theoretical line profiles (red) are compared with the observed profiles (histograms). The spectra are half-beam spaced. The intensity is given in the $T_{\rm mb}$ scale, where $\eta_{\rm mb}$ = 0.62. The absorption dip is centred on $\upsilon_{\rm LSR}$ = +3.3 km s^{-1}.

6.1. Age of the cloud

Based on dynamical considerations, dense and cold molecular cores are generally believed to be very young. However, a proper calibration of these qualitative age assessments is not readily achievable.

The chronometry of molecular clouds is a difficult task in general, but it may be achievable under special conditions. The hope is for "chemical clocks" that measure brief periods of transient times during the chemical evolution of the cloud.

In the dense core SM 1 in ρ Oph A, the highly unusual abundance ratio of O_2 to H_2O, i.e. $X(O_2)/X(H_2O) > 1$, indicates that the core is very young indeed; the age ranges from 5000 to 30 000 yr. Outside this narrow window, abundance ratios equal to or larger than unity are rarely ever encountered in the ISM and rapidly approach observed upper limiting values.

However, given the association of young stellar objects with the cloud would suggest that ρ Oph A has produced stars for at least one million years, unless the stellar sources that happen to move in front of the cloud are interlopers (at a rate of

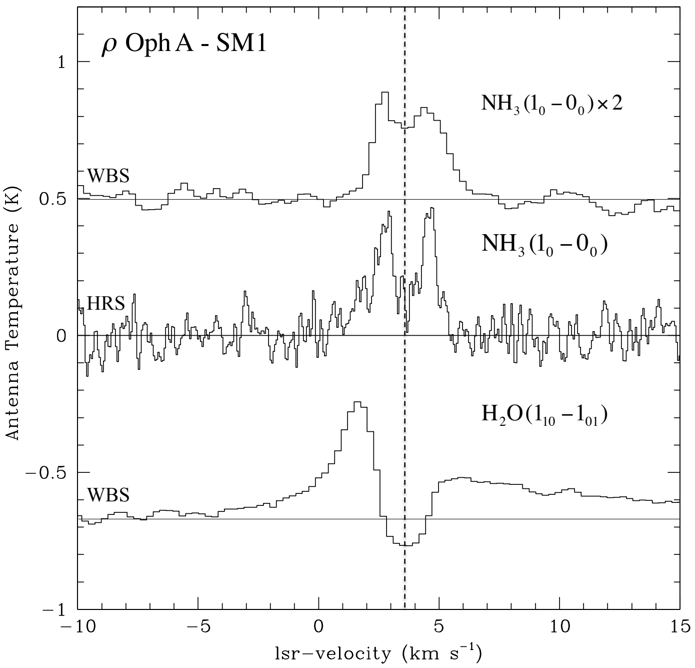

Fig. 11. Ground-state lines of NH_3 572 GHz and H_2O 557 GHz observed at the same time in the different sidebands of HIFI. Both lines show profiles characteristic of infall, but the NH_3 line lacks the high-velocity wings seen in water due to the VLA 1623 outflow. The middle figure shows the High Resolution Spectrometer (HRS) ammonia data, revealing the depth of the central absorption, and the other two the corresponding Wide Band Spectrometer (WBS) spectra at lower resolution.

1 pc per km s^{-1}) from other regions of the ρ Oph cloud. Proper motion data for the surroundings of ρ Oph A could help to settle this issue.

For the more distant F core (~0.8 pc, see Fig. A.1), and partially also for E, Ducourant et al. (2017) determined a mean proper motion that would correspond to an average lateral speed of 8 km s^{-1}. If also representative for the ρ Oph A neighbourhood, young objects (Class II to III) could have spilled in on time scales of less than 10^5 yr, providing an age estimate for the cloud core of that order.

6.2. Mass of the cloud

6.2.1. Dust opacity

It seems that it has generally been accepted that cloud masses are best determined from far-IR/submillimetre continuum observations, where the emission is likely optically thin and falls onto the Rayleigh-Jeans tail. Thus, to the first order, the only parameter to be determined appears to be the temperature of the dust.

In reality, however, the dust itself complicates things. In particular, the chemical composition and the size distribution of the grains determine the dust mass absorption coefficient κ_ν, which, as indicated by the subscript, is frequency dependent. This potentially distorts the spectrum of the cloud from being a pure black body. In Paper I, we examine this parameter in detail to determine its impact on the mass estimates. The most frequently exploited κ_ν values in the literature differ by factors of more than five.

6.2.2. Gas-to-dust mass ratio

To transform the estimated dust mass into total cloud mass requires the application of a gas–dust relationship, and an $m_{\rm gas}/m_{\rm dust} = 100$ is commonly assumed, often already implicitly in the value of κ.

However, in cold cores, a constant value of one hundred will most likely not be true everywhere since much of the gas-phase molecules will locally be frozen onto the dust grains, decreasing this ratio. Thus, potential freeze-out will invalidate commonly assumed calibrations, e.g. $X({\rm CO})/X({\rm H_2})$. In addition, gas and dust tracers will not measure the same parcels of material. For instance, in the cold core SM 1 in ρ Oph A, the gas-to-dust mass ratio is down by one order of magnitude from its canonical value of one hundred, i.e. $(m_{\rm gas}/m_{\rm dust})_{\rm SM\,1} \sim 10$; in addition, the projected distributions of the gas and dust do not coincide.

6.3. Star formation efficiency

Counting the stars that are associated with ρ Oph A is, in principle, a way to determine a limit to the cloud mass already converted into stars. Within a radius of $2\overset{\prime}{.}0$ (0.07 pc) around VLA 1623 A, the SIMBAD database lists 30 young stellar objects (4 TT + 26 classified as YSO). Only a few have an assigned spectral type, which means that proper mass assignments are basically impossible for the majority of objects. T Tauri stars have statistically about half a solar mass and assuming that to be the case for all objects probably provides an upper limit to the stellar mass ($M_{\rm TT} + M_{\rm YSO} \sim 15\,M_\odot$) in ρ Oph A. Similarly, assuming that the objects listed as YSOs have a mass of 0.1 $M_\odot$ yields a strict lower limit, so the total stellar mass probably falls within the range $4.5 < M_{\rm stars}/M_\odot < 15$.

The upper limit is roughly of the same order of magnitude as estimates of the present ρ Oph A mass (~5 to 35 $M_\odot$, Liseau et al. 2015). The star formation efficiency, $M_{\rm stars}/(M_{\rm stars} + M_{\rm cloud})$, in ρ Oph A is likely less than 50%; however, if all 30 stellar objects have actually formed in ρ Oph A, it could be as high as 20%. For the entire ρ Oph cloud complex (L 1688), Evans et al. (2009) determined an efficiency of 6%, much less than the ≥22% of Wilking et al. (1989), but in line with the value estimated by Liseau et al. (1995, 5–7%).

6.4. Evolution of the dust

In ρ Oph A, there is a clear trend of grain growth from the earliest to the latest phases of star formation (Fig. 13): big opacity exponents $\beta \sim 2$ mean small grains, whereas small $\beta \sim 0$ mean big grains. The dust grows from $a \lesssim 0.001\,\mu$m during the initial dark cloud phase to $a \gtrsim 100\,\mu$m towards the later T Tauri and ZAMS phases. At intermediate times, i.e. during the protostellar and protoplanetary stages, grain sizes vary between 0.1 and 10 μm. Respective grain size distribution parameters p, where $dn(a) \propto a^{-p}\,da$, are 4.5−5 (Class−1 and 0), 3.5−4 (Class I and II), and 3 (Class III).

Further quantitative assessment is hampered by the poorly constrained early evolutionary time scales. However, if we assume currently adopted ages (e.g. Evans et al. 2009), the data can be fit by an exponential, as shown in Fig. 13, from which we can infer that the observed dust is dominated by a population of very small grains at the earliest times (starless cores and dynamical collapse) up to 50–100 thousand years. After that, grains grow predominantly in circumstellar discs, as the relative contribution to the far-IR/submm emission from these grains continues to increase.

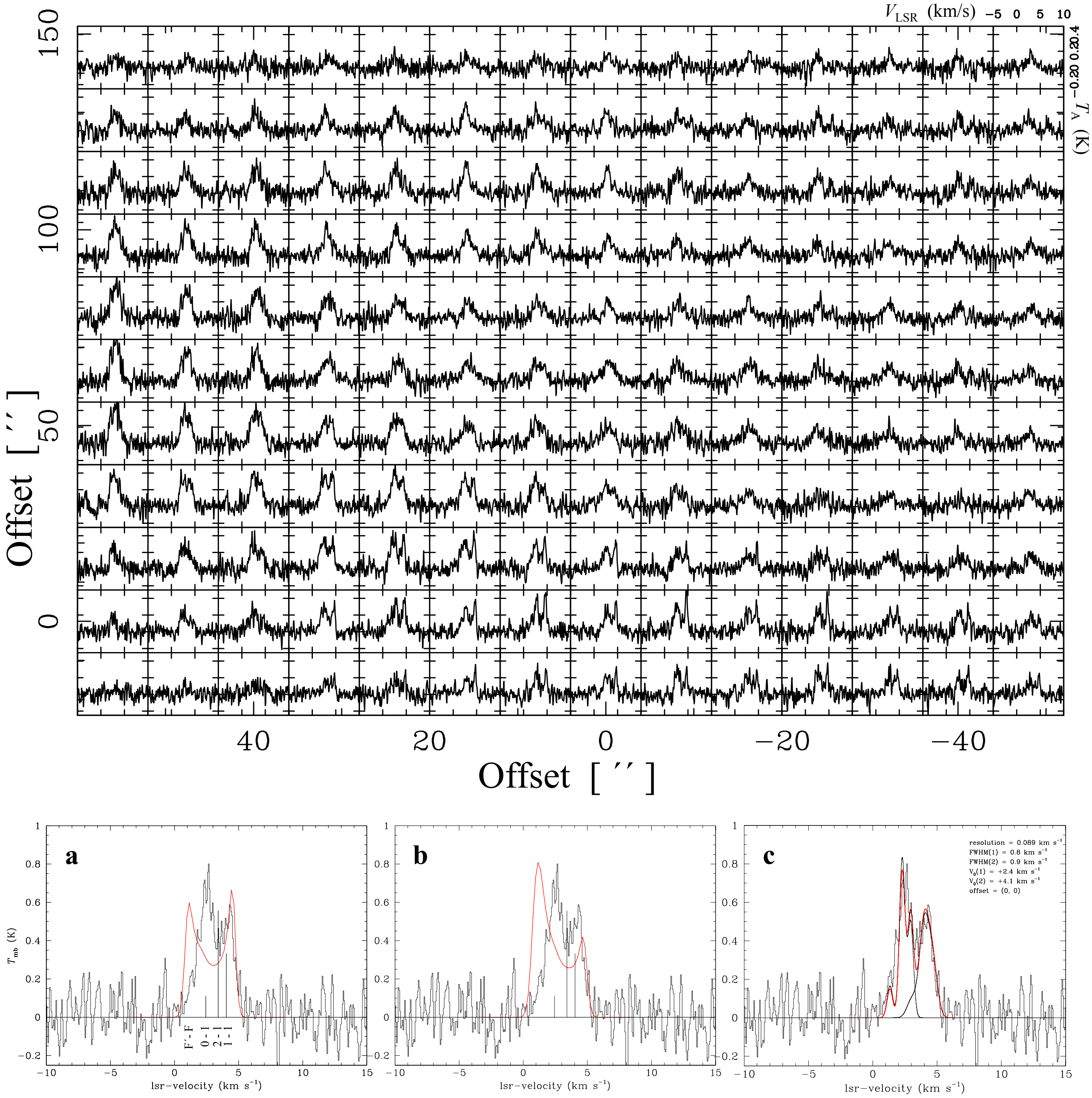

Fig. 12. *Upper*: part of the observed *Herschel*-HIFI map in the ground state line of o-NH_3; the scales are indicated in the *upper right corner*. *Lower*: observed high-resolution (HRS) NH_3 (1_0−0_0) line profiles towards SM 1N shown as histograms. The red lines show a static BE model in *a*), whereas in *b*) an infall model is shown. The positions of the hfs components are shown as vertical bars, the lengths of which are normalized to 1.0, and their quantum numbers are indicated in *a* (see Appendix B). Panel *c* shows the results of Gaussian hfs profile fitting for two velocity components, the parameters of which are inscribed.

6.5. Protostellar mass infall

Scientists with a talent for poetry once called the discovery of a collapsing protostar "the holy grail of star formation", and indeed, the identification of a true collapsing protostar in ρ Oph A appeared initially very promising (Ashby et al. 2000). Like these authors, we used the observed H_2O 557 GHz line to fit its profile with a protostellar infall model and radiative transfer calculations, disregarding the extended line wings which were attributed to the VLA 1623 outflow by Ashby et al. (2000). In addition, we also applied the same model to the observed NH_3 (1_0−0_0) lines. These are not contaminated with outflow emission in the line wings.

These models did indeed recover the infall signature imprinted in the H_2O line profile. However, our higher quality data and more advanced theoretical modelling could not uniquely confirm the proposed protostellar scenario as the observations show the infall profile over a much larger region than the model with the slightly larger than 1 $M_\odot$ potential could account for.

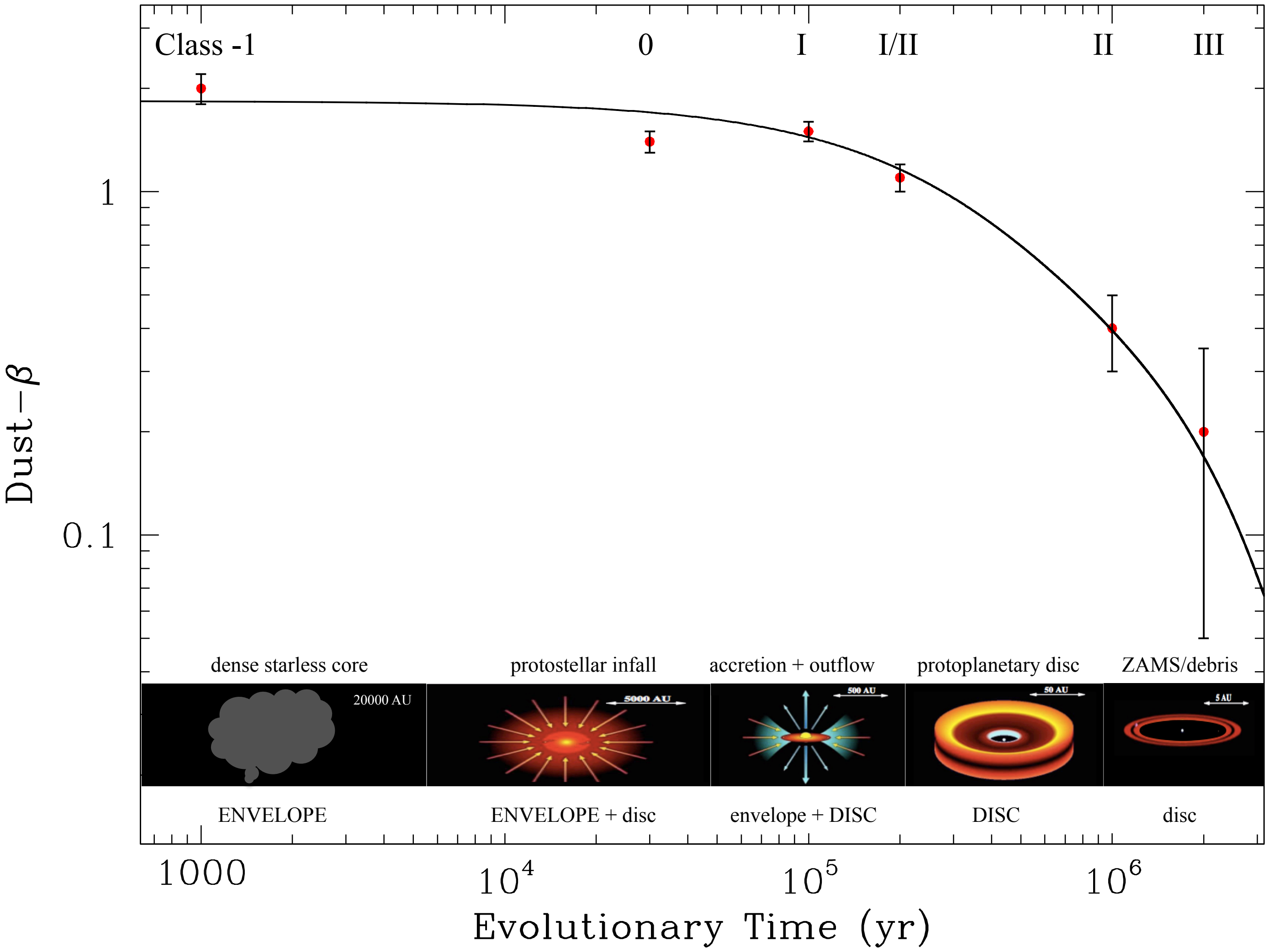

Fig. 13. Dust opacity index β as a function of evolutionary time of star formation. β describes the frequency dependence of the dust opacity $\kappa_{\nu,\,\mathrm{dust}}$ in the Rayleigh-Jeans regime according to the power law $\kappa_{\nu,\,\mathrm{dust}} \propto \nu^{\beta}$. The cartoons are from McCoughrean/NASA/JWST. The major contributor to the dust emission at the various stages is indicated below the icons and the nature of the objects above them. The importance of a given contributor to the far-IR/submm emission is expressed in upper and lower case letters, respectively. The common nomenclature of stellar formation, labelled Class -1 through Class III, is shown above the data points with their 1σ errors. The line through the data points is an analytical fit of the form $\beta(t) = a_1\ \exp(-\gamma_1 t/\tau) + a_2\ \exp(-\gamma_2 t/\tau)$, where $\tau = 5 \times 10^4$ yr is a characteristic time scale, after which increased grain growth occurs in discs.

6.6. *PDR dynamics*

ρ Oph A is sandwiched between the far-UV radiation fields from two B-type stars, one to the east and the other to the far west. The PDR parameter G_0/n ranges from 0.001 to 0.01, considerably lower than for commonly studied PDRs. The spherical shell morphology of the eastern region could suggest that the dark core has been shaped and compressed by the radiation fields. However, currently we do not find convincing observational evidence for a strong pressure gradient at the PDR-border. Rather, it seems that an equilibrium situation has been achieved that has settled the gas into a quasi-static, clumpy configuration.

Acknowledgements. We thank the Swedish National Space Board (SNSB) for its continued support of our *Herschel* projects. The contributions to this project in its initial phase by Drs. Per Bergman, Alexis Brandeker, and Michael Olberg are acknowledged. Dr. Tim-Oliver Husser and Dr. Emanuele Bertone are thanked for providing high-resolution spectra of stellar model atmospheres.

References

Alexander, M. H., & Dagdigian, P. J. 1985, J. Chem. Phys., 83, 2191
Ashby, M. L. N., Bergin, E. A., Plume, R., et al. 2000, ApJ, 539, L119
Asplund, M., Grevesse, N., Sauval, A. J., & Scott, P. 2009, ARA&A, 47, 481
Bergman, P., Parise, B., Liseau, R., & Larsson, B. 2011a, A&A, 527, A39
Bergman, P., Parise, B., Liseau, R., et al. 2011b, A&A, 531, L8
Bieler, A., Altwegg, K., Balsiger, H., et al. 2015, Nature, 526, 678
Bjerkeli, P., Liseau, R., Larsson, B., et al. 2012, A&A, 546, A29
Bohlin, R. C., Savage, B. D., & Drake, J. F. 1978, ApJ, 224, 132
Bonnor, W. B. 1957, MNRAS, 117, 104
Bontemps, S., André, P., Kaas, A. A., et al. 2001, A&A, 372, 173
Booth, R. S., Delgado, G., Hagstrom, M., et al. 1989, A&A, 216, 315
Canning, R. E. A., Ferland, G. J., Fabian, A. C., et al. 2016, MNRAS, 455, 3042
Castelli, F., & Kurucz, R. L. 2004, ArXiv e-prints [`arXiv:astro-ph/0405087`]
Cazzoli, G., Dore, L., & Puzzarini, C. 2009, A&A, 507, 1707
Cesarsky, C. J., Abergel, A., Agnese, P., et al. 1996, A&A, 315, L32
Chen, J., Zhang, Y.-H., & Zhou, T.-C. 1998, Chin. Astron. Astrophys., 22, 113
Clegg, P. E., Ade, P. A. R., Armand, C., et al. 1996, A&A, 315, L38
Danby, G., Flower, D. R., Valiron, P., Schilke, P., & Walmsley, C. M. 1988, MNRAS, 235, 229

de Graauw, T., Helmich, F. P., Phillips, T. G., et al. 2010, A&A, 518, L6
Di Francesco, J., André, P., & Myers, P. C. 2004, ApJ, 617, 425
Du, F., Parise, B., & Bergman, P. 2012a, A&A, 538, A91
Du, F., Parise, B., & Bergman, P. 2012b, A&A, 544, C4
Ducourant, C., Teixeira, R., Krone-Martins, A., et al. 2017, A&A, 597, A90
Ebert, R. 1957, Zeitschrift für Astrophysik, 42, 263
Evans, II, N. J., Dunham, M. M., Jørgensen, J. K., et al. 2009, ApJS, 181, 321
Faure, A., Crimier, N., Ceccarelli, C., et al. 2007, A&A, 472, 1029
Faure, A., Hily-Blant, P., Le Gal, R., Rist, C., & Pineau des Forêts, G. 2013, ApJ, 770, L2
Foster, P. N., & Chevalier, R. A. 1993, ApJ, 416, 303
Friesen, R. K., Di Francesco, J., Bourke, T. L., et al. 2014, ApJ, 797, 27
Frisk, U., Hagström, M., Ala-Laurinaho, J., et al. 2003, A&A, 402, L27
Gagné, M., Skinner, S. L., & Daniel, K. J. 2004, ApJ, 613, 393
Goldsmith, P. F., Melnick, G. J., Bergin, E. A., et al. 2000, ApJ, 539, L123
Goldsmith, P. F., Li, D., Bergin, E. A., et al. 2002, ApJ, 576, 814
He, J., Shi, J., Hopkins, T., Vidali, G., & Kaufman, M. J. 2015, ApJ, 801, 120
Hjalmarson, Å., Frisk, U., Olberg, M., et al. 2003, A&A, 402, L39
Hollenbach, D. J., & Tielens, A. G. G. M. 1999, Rev. Mod. Phys., 71, 173
Hollenbach, D., Kaufman, M. J., Bergin, E. A., & Melnick, G. J. 2009, ApJ, 690, 1497
Justtanont, K., Liseau, R., & Larsson, B. 2008, in IAU Symp. 251, eds. S. Kwok, & S. Sanford, 227
Kamazaki, T., Saito, M., Hirano, N., Umemoto, T., & Kawabe, R. 2003, ApJ, 584, 357
Larsson, B., Liseau, R., Men'shchikov, A. B., et al. 2000, A&A, 363, 253
Larsson, B., Liseau, R., Bergman, P., et al. 2003, A&A, 402, L69
Larsson, B., Liseau, R., Pagani, L., et al. 2007, A&A, 466, 999
Le Bourlot, J., Le Petit, F., Pinto, C., Roueff, E., & Roy, F. 2012, A&A, 541, A76
Le Petit, F., Nehmé, C., Le Bourlot, J., & Roueff, E. 2006, ApJS, 164, 506
Le Petit, F., Barzel, B., Biham, O., Roueff, E., & Le Bourlot, J. 2009, A&A, 505, 1153
Liseau, R., & Justtanont, K. 2009, A&A, 499, 799
Liseau, R., Lorenzetti, D., Molinari, S., et al. 1995, A&A, 300, 493
Liseau, R., White, G. J., Larsson, B., et al. 1999, A&A, 344, 342
Liseau, R., Larsson, B., Brandeker, A., et al. 2003, A&A, 402, L73
Liseau, R., Justtanont, K., & Tielens, A. G. G. M. 2006, A&A, 446, 561
Liseau, R., Larsson, B., Bergman, P., et al. 2010, A&A, 510, A98
Liseau, R., Goldsmith, P. F., Larsson, B., et al. 2012, A&A, 541, A73
Liseau, R., Larsson, B., Lunttila, T., et al. 2015, A&A, 578, A131 (Paper I)
Loinard, L., Torres, R. M., Mioduszewski, A. J., & Rodríguez, L. F. 2008, ApJ, 675, L29
Loren, R. B., Wootten, A., & Wilking, B. A. 1990, ApJ, 365, 269
Maercker, M., Schöier, F. L., Olofsson, H., Bergman, P., & Ramstedt, S. 2008, A&A, 479, 779
Melnick, G. J., & Kaufman, M. J. 2015, ApJ, 806, 227
Melnick, G. J., Stauffer, J. R., Ashby, M. L. N., et al. 2000, ApJ, 539, L77
Neufeld, D. A., Nisini, B., Giannini, T., et al. 2009, ApJ, 706, 170
Nordh, H. L., von Schéele, F., Frisk, U., et al. 2003, A&A, 402, L21
Olberg, M., Frisk, U., Lecacheux, A., et al. 2003, A&A, 402, L35
Pagani, L., Olofsson, A. O. H., Bergman, P., et al. 2003, A&A, 402, L77
Parise, B., Bergman, P., & Du, F. 2012, A&A, 541, L11
Pilbratt, G. L., Riedinger, J. R., Passvogel, T., et al. 2010, A&A, 518, L1
Poglitsch, A., Waelkens, C., Geis, N., et al. 2010, A&A, 518, L2
Poynter, R. L., & Kakar, R. K. 1975, ApJS, 29, 87
Punanova, A., Caselli, P., Pon, A., Belloche, A., & André, P. 2016, A&A, 587, A118
Roelfsema, P. R., Helmich, F. P., Teyssier, D., et al. 2012, A&A, 537, A17
Rubin, M., Altwegg, K., van Dishoeck, E. F., & Schwehm, G. 2015, ApJ, 815, L11
Sandqvist, A., Bergman, P., Black, J. H., et al. 2003, A&A, 402, L63
Sandqvist, A., Larsson, B., Hjalmarson, Å., et al. 2015, A&A, 584, A118
Schöier, F. L., van der Tak, F. F. S., van Dishoeck, E. F., & Black, J. H. 2005, A&A, 432, 369
Snell, R. L., Howe, J. E., Ashby, M. L. N., et al. 2000, ApJ, 539, L101
Taquet, V., Furuya, K., Walsh, C., & van Dishoeck, E. F. 2016, MNRAS, 462, S99
Tielens, A. G. G. M. 2005, The Physics and Chemistry of the Interstellar Medium (Cambridge University Press)
Townes, C. H., & Schawlow, A. L. 1955, Microwave Spectroscopy (New York: McGraw-Hill)
Ulich, B. L., & Haas, R. W. 1976, ApJS, 30, 247
Umemoto, T., Kamazaki, T., Sunada, K., Kitamura, Y., & Hasegawa, T. 2002, in 8th Asian-Pacific Regional Meeting, eds. S. Ikeuchi, J. Hearnshaw, & T. Hanawa, II, 229
van Dishoeck, E. F., Kristensen, L. E., Benz, A. O., et al. 2011, PASP, 123, 138
White, G. J., Drabek-Maunder, E., Rosolowsky, E., et al. 2015, MNRAS, 447, 1996
Wilking, B. A., & Lada, C. J. 1983, ApJ, 274, 698
Wilking, B. A., Lada, C. J., & Young, E. T. 1989, ApJ, 340, 823
Wilking, B. A., Gagné, M., & Allen, L. E. 2008, Star Formation in the ρ Ophiuchi Molecular Cloud, ed. B. Reipurth, 351
Wirström, E. S., Charnley, S. B., Cordiner, M. A., & Ceccarelli, C. 2016, ApJ, 830, 102
Yıldız, U. A., Acharyya, K., Goldsmith, P. F., et al. 2013, A&A, 558, A58

Appendix A: Odin observations of the ρ Oph cloud

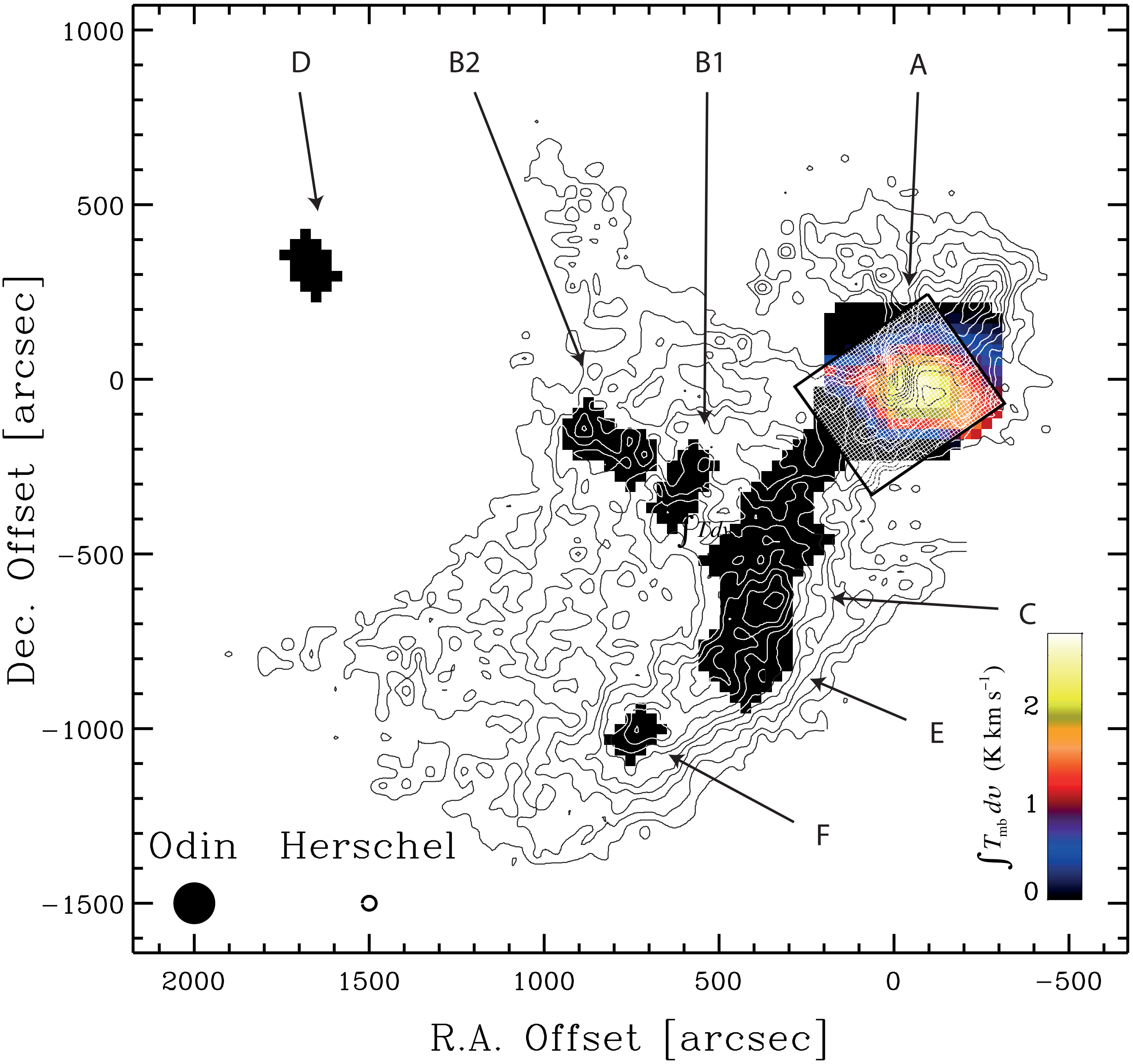

Fig. A.1. Spectral line image of the ρ Oph cloud (L 1688) in the H_2O ($1_{10}-1_{01}$) 557 GHz line obtained by Odin with its 2′ beam, which is indicated to scale in the *lower left corner*. The colour-coding for the integrated intensity $\int T_{\rm mb}\, dv$ is shown by the scale bar in the *lower right*. The cores A through F are labelled, and the Odin data are superposed onto the contours of integrated $C^{18}O$ ($J = 1-0$) emission from Umemoto et al. (2002). The J2000-coordinates of the (0, 0) position are RA = $16^h26^m24\overset{s}{.}6$ and Dec = −24°23′54″ and offsets are in seconds of arc. The *Herschel* beam at 557 GHz is shown next to that of Odin and the inclined, semi-transparent rectangle outlines the region mapped with HIFI.

Prior to *Herschel*, we had mapped the ρ Oph cloud in the H_2O ($1_{10}-1_{01}$) line at 557 GHz with the spectrometers aboard the Odin spacecraft (Frisk et al. 2003; Nordh et al. 2003; Olberg et al. 2003). Between 2003 and 2006, the ρ Oph cloud was mapped in the H_2O 557 GHz line during several observing runs (see Table A.1). The coordinates of the map centre, i.e. at offset position (0, 0), were RA = $16^h26^m24\overset{s}{.}6$ and Dec = −24°23′54″ (J2000). At the frequency of the H_2O ($1_{10}-1_{01}$) transition, the beam width of Odin is 2′ (HPBW) and for ρ Oph A, in particular, the spatial sampling was at about the Nyquist frequency, with relative offsets in 60″ steps.

The front- and backends (Frisk et al. 2003; Olberg et al. 2003) were, respectively, the 555 B1 receiver and either of the two digital autocorrelators (ACs) with a bandwidth of 400 MHz. The channel resolution was 0.5 MHz, corresponding to 0.27 km s^{-1} and implying a velocity resolution of ~0.5 km s^{-1}. However, for the large map of 2005 and the outflow strip scan of 2006, two H_2O receivers were used and the backends were the other autocorrelator (AC2 in 2005) and the acousto-optical spectrometer (AOS in 2006). The observing mode was always Dicke-switching, with the 4$\overset{\circ}{.}$4 sky-beam pointing off by 42° (Olberg et al. 2003).

Table A.1. Journal of Odin H_2O 557 GHz observations.

Year	Date	Orbits	Used Orbits	Integration (h)	Pointings	Source
2003	February 1–24	10 577–10 918	120	36.2	12	ρ Oph A
2003	August 8–18	13 372–13 527	83	20.9	4	ρ Oph A
2004	January 31	15 992–16 006	11	3.3	2	ρ Oph A
2004	August 1–12	18 730–18 901	86	18.9	3 + 5	ρ Oph B1, B2
2005	July 31–October 1	24 181–25 100	394	73.5 + 109.4[a]	51	ρ Oph A to F
2006	February 2–March 2	26 956–27 370	198	75.4	12	ρ Oph A
2006	August 26–September 18	30 016–30 357	142	48.3 + 46.6[b]	3	VLA 16293
Total			1034	432.5	92	

Notes. [(a)] OB + OC; [(b)] VLA Outflow: AOS + AC.

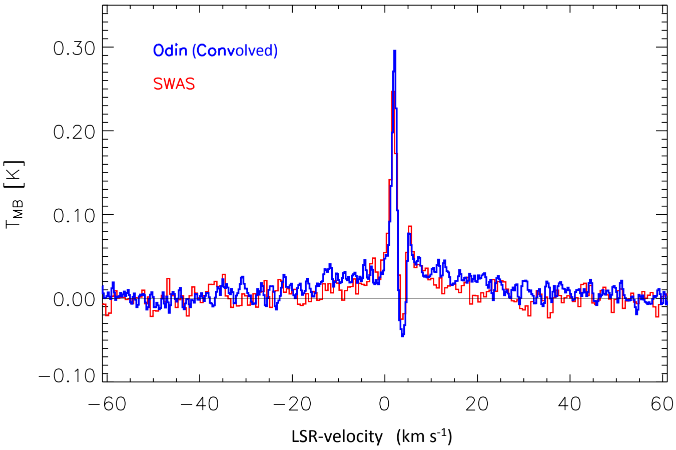

Fig. A.2. H_2O 557 GHz spectra of ρ Oph A obtained by SWAS and Odin. For this comparison, the Odin data have been convolved into the larger SWAS beam and are shown in blue, whereas the SWAS spectrum at two times lower frequency resolution is displayed in red. The comparison reveals a high degree of consistency and shows the high-velocity wings, traceable to at least ±30 km s^{-1} relative to the systemic Doppler velocity.

During the mapping procedure in 2005, all 51 positions were observed once per satellite revolution in a raster scan mode. Individual spectral scans were 5 s each. An "off-position", supposedly free from molecular line emission, was also observed once per revolution. The total on-source time spent on every observed point was on average 3.5 h for the cores C to F. For the B cores, the average observing time was 6 h on-source. Finally, for ρ Oph A, this time was about 12 h.

The system noise temperature $T_{\rm sys}$ was within the range 3300 K to 3400 K (single sideband, SSB). Examination of all the position data reveals that the relative pointing accuracy is better than 2″ (rms scatter) for any individual position and better than 5″ for the overall final map (<4% of the Odin beam width).

The basic data reduction procedure is described by Olberg et al. (2003). The appropriate equations are given in that paper and will not be repeated here. The spectrum of the off-position, obtained once per revolution, was used to monitor the reduction of the Dicke-switched spectra along the pipeline. This procedure assured that the final results are reliable. The absolute accuracy of the intensity scale is believed to be better than 10% (Hjalmarson et al. 2003). Comparison with the data obtained by SWAS shows excellent agreement (Fig. A.2).

Due to the relatively low orbit of Odin, astronomical sources are generally occulted by the Earth. As a consequence, Odin "is observing" through the Earth's atmosphere twice per orbital revolution, i.e. during ingress and egress phases of the eclipse (see Fig. 2 in Nordh et al. 2003). This circumstance has an advantage, as the telluric ground state line of H_2O at 556.936 GHz permits a highly accurate frequency calibration (Larsson et al. 2003). In fact, the final accuracy is better than half a channel width ($\delta\upsilon < 0.14$ km s^{-1}), which takes into account the averaging of all the scans for the individual map positions, corrected for the motion of the Earth and the satellite in the local standard of rest (LSR) velocity scale.

Table A.2. Odin H_2O 557 GHz results for ρ Oph cores A through F.

ρ Oph Core	Pointings	Integration (h)	$T_{\rm rms}^{\rm point}$ (mK)	$T_{\rm rms}^{\rm ave}$ (mK)
A	35	155	20	6
B1	3	3.6	49	49
B2	5	31.0	39	18
C	16	64.0	39	10
D	2	6.4	41	29
E	9	36.0	40	13
F	2	3.0	66	47

With Odin, the average of the scans for each position results in a 70-point map for ortho-water with 60″ spacing of the dense cores A to F. As can be seen in Fig. A.1, no water emission was detected towards any of the cores except towards ρ Oph A. Furthermore, Table A.2 shows that the overall achieved sensitivity is about 40 mK per pointing[8]. In individual cases, e.g. core C, an rms noise temperature of $T_{\rm rms} = 10$ mK is obtained when averaging the measurements for all positions towards a single core. In Table A.2, the basic results are summarized. Of the seven cores observed, only ρ Oph A was clearly detected (Fig. A.1). The ground-state transition of ortho-water in ρ Oph A has also been observed with SWAS (Ashby et al. 2000; Snell et al. 2000). The Odin and SWAS data are in excellent agreement (Fig. A.2).

Appendix B: Hyperfine structure in NH_3

The rotational levels of NH_3 are hyperfine-split due to quadrupole interaction (see Fig. B.1). The relative line strengths

---

[8] The conversion from K to Jy is about 0.02 mK/Jy (Sandqvist et al. 2003).

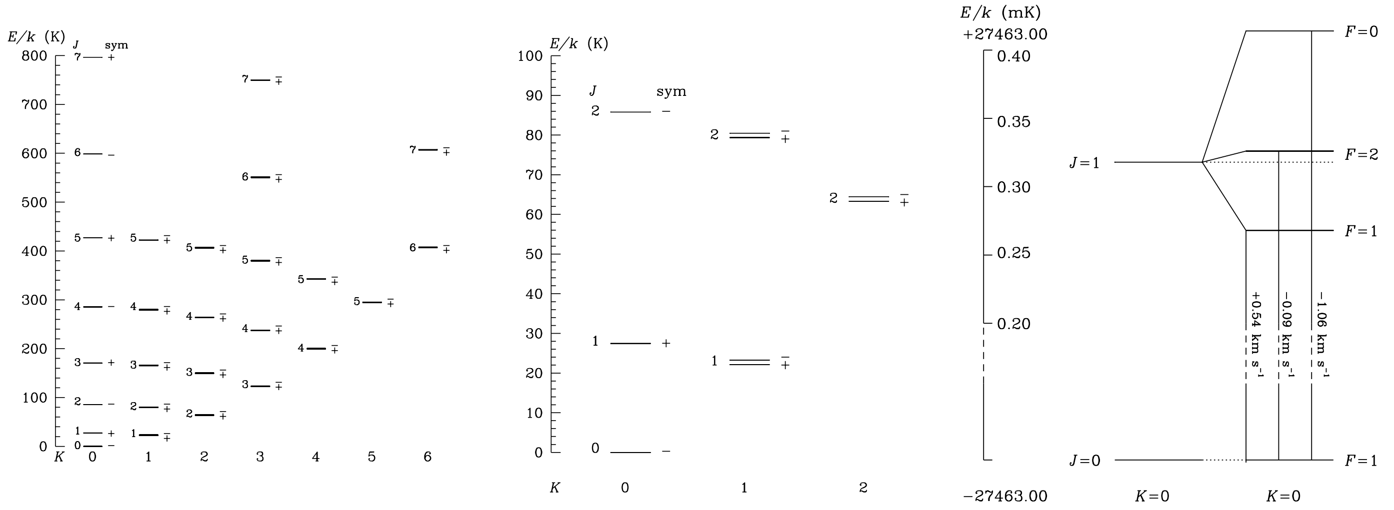

Fig. B.1. *Left*: rotational energy levels of NH$_3$ (see the LAMDA data bank, Schöier et al. 2005). Energies up to 800 K are given for the ortho-NH$_3$ states ($K = 0$ or K = multiple of 3), whereas these are roughly half for para-NH$_3$ ($K \neq 0$ and $K \neq$ multiple of 3). All levels are plotted to scale, rendering the inversion splittings unresolved. *Middle*: same as left frame, but for energies below 100 K. For symmetry reasons, half of the inversion levels do not exist for $K = 0$. In this panel, the inversion levels, shown to scale, are resolved. *Right*: hyperfine splitting, due to quadrupole interaction, of the ($J = 1$, $K = 0$) level is shown. The resulting shifts, in km s^{-1}, for the NH$_3$ (1_0–0_0) line are indicated next to the components. The drawing is to scale and energies are in milli-Kelvin.

in equilibrium are

$$S^{\rm hfs}_{\rm ul} = \left[(2J_{\rm u}+1)(2J_{\rm l}+1)\begin{pmatrix} J_{\rm l} & 1 & J_{\rm u} \\ K & 0 & -K \end{pmatrix}^2\right] \times \left[(2F_{\rm l}+1)(2F_{\rm u}+1)\begin{Bmatrix} J_{\rm u} & F_{\rm u} & I \\ F_{\rm l} & J_{\rm l} & 1 \end{Bmatrix}^2\right], \qquad \text{(B.1)}$$

where the first factor in square brackets is the line strength $S_{\rm ul}$ for rotational transitions ($J_{\rm u}$, $K \rightarrow J_{\rm l}$, K). The relative strengths for the hyperfine transitions of the (1, 0 → 0, 0) line are given in Table B.1.

Ammonia comes in two “flavors”, namely ortho-NH$_3$ (or A-state) and para-NH$_3$ (or E-state). The statistical weights for the rotational levels are $g_J\, g_I$, where $g_J = 2J + 1$ and where g_I refers to the spin of the three hydrogen nuclei, $I = I_{\rm H}$. These are (Townes & Schawlow 1955)

A-state or ortho-NH$_3$: $I = \frac{3}{2}$; $g_I = \frac{1}{3}(2I+1)(2I-1)I = 4$
E-state or para-NH$_3$: $I = \frac{1}{2}$; $g_I = \frac{1}{3}(2I+1)(4I^2+4I) = 2$

so that the equilibrium ratio of the weights of the ortho-to-para states is $o/p = 2$. At high temperatures, $o/p = 1$ (Faure et al. 2013). For the ortho-states, K takes the values $K = 3n$, $n = 0, 1, 2, \ldots, N$ and for the para-states all the others. Therefore, the results for the (1_0–0_0) ortho-line reported here are not necessarily directly related to those for the inversion lines, e.g. (1, 1), (2, 2), etc., that have been commonly cited in the literature.

The statistical weights of the hfs lines are $g_F = 2F + 1$, and the Einstein A-values are obtained from

$$A(J, J-1)_{K,\pm} = \frac{64\,\pi^4 \nu^3 \mu^2}{3\,hc^3}\,\frac{J^2 - K^2}{J(2J+1)}. \qquad \text{(B.2)}$$

For NH$_3$, the dipole moment $\mu = 1.476 \pm 0.002$ Debye (Poynter & Kakar 1975). The hfs levels and their weighted Einstein As have been implemented in the ALI programme, which includes 49 levels, up to ~600 K, and 104 radiative transitions. When $\tau \geq 1$ at line centre, the relative contributions of the hfs lines will be different from those in equilibrium. Line overlap is explicitly accounted for by the transfer code.

Table B.1. Data for NH$_3$ quadrupole interaction for $K = 0$, $J = 0$.

hfs $F' - F$	Frequency (MHz)	$\Delta\upsilon_{F'}$ (km s^{-1})	$(E_0 - E_{F'})/k$ (K)	Relative strength
1–1	572 497.1247	+0.542	$+5.0 \times 10^{-5}$	0.333
2–1	572 498.3391	−0.094	-8.1×10^{-6}	0.556
0–1	572 500.1914	−1.064	-9.7×10^{-5}	0.111

Notes. Adopted centre frequency is ν_0 = 572 498.160 MHz and eqQ = −4.08983 MHz (Cazzoli et al. 2009).

Collision rate constants $C_{\rm u\leftrightarrow l}$ for the hfs transitions $J_{\rm u\leftrightarrow l} = 1 \leftrightarrow 0$, $K = 0$ have been published by Chen et al. (1998). However, for the sake of consistency, we computed the collision rates for the hfs transition among all J, K levels according to the prescription given by Alexander & Dagdigian (1985). These approximations are valid within a given K-ladder (see e.g. Fig. B.2). For cross-K transitions we simply adopted the data provided by Danby et al. (1988). Included are 1162 transitions for eight temperatures in the range 15 to 300 K.

Appendix C: CS line maps with the Swedish ESO Submillimetre Telescope

Mapping observations in CS (2–1), (3–2), and (5–4) were performed at the 15 m Swedish ESO Submillimetre Telescope (SEST; Booth et al. 1989) during 1996 and 1997 (Table C.1). As frontends we used SIS-mixer receivers and as backend a 1000-channel acousto-optical spectrometer (AOS) with 43 kHz resolution. The observations were performed in frequency switching mode with a frequency throw of 7 MHz for the 100 and 150 GHz observations and of 15 MHz for those at 250 GHz. At these frequencies system noise temperatures were $T_{\rm sys} \sim 150$, 200, and 400 K, respectively.

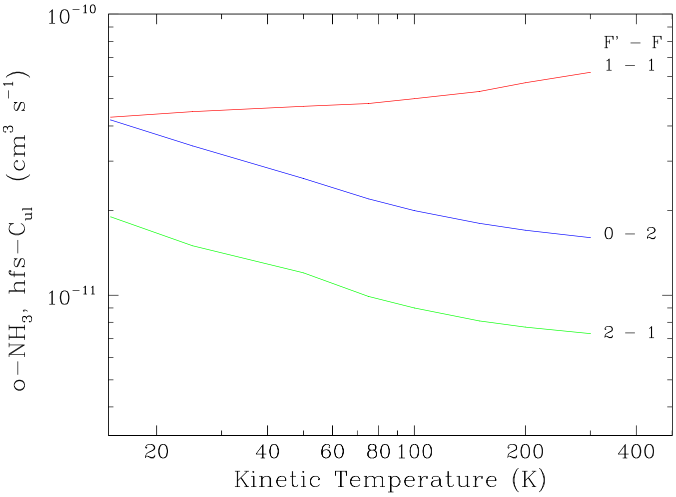

Fig. B.2. Rate coefficients for collisional de-excitation $C_{\rm ul}$ for hfs transitions of J, K = 1, 0–0, 0 (see text).

The pointing of the telescope was regularly checked using stellar SiO masers and found to be better than 3″ rms. The (2–1) and (3–2) maps were obtained simultaneously with two receivers and these covered an area of $5' \times 5'$. In the (5–4) line, a $\Delta\alpha \times \Delta\delta = 3' \times 2'$ was obtained. The data are internally chopper-wheel calibrated in the $T_{\rm A}^*$-scale (Ulich & Haas 1976) and as celestial calibrator, we used M 17 SW (RA = 18h 20m 23.1s, Dec = −16°11′43″, J2000.0). Repeated observations on different occasions resulted in stable intensities of the lines within 4 to 5%. The $T_{\rm mb}$ values were obtained by applying the main beam efficiencies, $\eta_{\rm mb}$, provided in Table C.1.

Table C.1. Instrumental reference: SEST.

CS $J+1-J$	ν_0 (GHz)	$E_{\rm up}/k$ (K)	$A_{\rm ul}$ (s^{-1})	$HPBW$ (″)	$\eta_{\rm mb}$
2–1	97.9809533	7	1.68×10^{-5}	50	0.73
3–2	146.9690287	14	6.06×10^{-5}	33	0.67
5–4	244.9355565	35	2.98×10^{-4}	20	0.60

Standard data reduction techniques were applied in Class and with the locally available software package `xs`[9], involving folding of the spectra, fitting and subtracting base lines, and averaging multiple scans for the same position.

Appendix D: Synopsis of gas observations: lines and telescopes

In Table D.1 we provide an overview of the spectral lines that have been observed and analysed in Papers I and II.

Table D.1. Summary of gas observations.

Atom or Molecule	Quantum Numbers	Frequency (GHz)	Upper level Energy (K)	Observing Facility
H_2	J = 2–0, S(2)	244×10^6	1682	ISO-CAM CVF
	J = 3–1, S(3)	310×10^6	2503	ISO-CAM CVF
	J = 5–3, S(5)	433×10^6	4586	ISO-CAM CVF
O	J = 1–2	4744	228	*Herschel*-PACS
	J = 0–1	2010	326	*Herschel*-PACS
CH^+	J = 2–1	1669	153	*Herschel*-HIFI
NH_3	J = 1–0, K = 0–0	572	27	Odin, *Herschel*-HIFI
H_2O	J = 1–1, $K_{\rm a}$ = 1–0, $K_{\rm c}$ = 0–1	556	37	Odin, *Herschel*-HIFI
	J = 2–1, $K_{\rm a}$ = 1–0, $K_{\rm c}$ = 2–1	1669	114	*Herschel*-PACS, *Herschel*-HIFI
C_2H	J = 17/2–15/2, N = 9–8	785	208	*Herschel*-HIFI
	J = 19/2–17/2, N = 9–8	785	208	*Herschel*-HIFI
$^{13}C^{16}O$	J = 7–6	771	148	*Herschel*-HIFI
$^{12}C^{17}O$	J = 7–6	786	151	*Herschel*-HIFI
N_2H^+	J = 3–2	279	28	APEX
	J = 6–5	558	94	*Herschel*-HIFI
O_2	J = 1–1, N = 1–0	118	6	Odin
	J = 3–1, N = 3–2	487	26	*Herschel*-HIFI
	J = 5–3, N = 4–4	773	61	*Herschel*-HIFI
$^{12}C^{32}S$	J = 2–1	97	7	SEST
	J = 3–2	146	14	SEST
	J = 5–4	244	35	SEST
	J = 10–9	489	129	*Herschel*-HIFI

---

[9] `ftp://yggdrasil.oso.chalmers.se/pub/xs/`